

# Methane Hydrates and Climate Change

## Bachelor Thesis



Ingeborg Kvalheim (s144352)  
 Marte Teksum Haugland (s136435)  
 Supervisor: Jens Olaf Pepke Pedersen  
 June 2017

# 1 Abstract

Methane hydrates are natural, crystal-like structures composed of  $\text{H}_2\text{O}$  and predominantly the greenhouse gas  $\text{CH}_4$ . They mainly exist under high pressure and low temperature conditions in two main sedimentary domains: in permafrost and in ocean sediments.  $\text{CH}_4$  of a substantial abundance is sequestered in hydrate form, and contributes to a significant sink of carbon in the carbon cycle. However, methane hydrates are susceptible to climate change, as the hydrate stability is a function of pressure, temperature and salinity conditions. With sufficient bottom ocean temperature rise, the methane hydrates will dissociate and release free and dissolved  $\text{CH}_4$  gas to the sediment, water column and eventually atmosphere. Implementation of a methane hydrate segment and IPCC scenarios in the DCESS- Earth System Model, allows evaluation of the change in global hydrate inventory and associated effects on atmospheric and oceanic conditions due to climate change. We find that between 0.04 % (B1 3°C) and 0.6 % (A2 5°C) of the global hydrate inventory of 1800 Gt C dissociates in a simulation period starting in 1750 and ending in 2250. All dissociating hydrate exists at 400 meters to 900 meters depth in the upper continental slope, which is therefore evaluated to be highly susceptible to climate change. The  $\text{CH}_4$  release range is between 0.90 Gt C and 10.90 Gt C during the 500 year simulation. In none of the scenarios is the release substantial enough to lead to local ocean anoxia and acidification. In the A2(5°C) scenario, 0.5°C of the total temperature rise of 8.9°C is attributed to gas hydrate dissociation and the  $\text{CO}_2$  concentration is 1.03 times higher than a model run without any dissociated  $\text{CH}_4$ . In 2100, the  $\text{CH}_4$  concentration in the atmosphere will be 8.6 atm in the A2(5°C) scenario, which is the most severe scenario, and 3.8 atm in the B1(3°C) scenario, which is the mildest. The B1 scenario has a negligible effect on atmospheric greenhouse gas concentrations. The amount of methane released from melting hydrates by 2100 is small and will not have a major impact on the global climate. The total release of  $\text{CH}_4$  in any IPCC scenario is minimal compared to the contemporary anthropogenic release of  $\text{CH}_4$ .

## 2 Preface

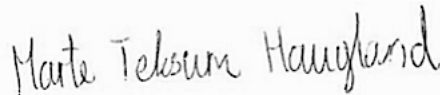
This bachelor report is our final project of the bachelor degree 'Vand, bioressourcer og miljø management' at the Technical University of Denmark, DTU. The project has been conducted as a collaboration between DTU Polar of the National Space Institute and the Environmental Engineering department. It was developed through the 13-week period of the spring semester 2017 and is credited 20 ECTS per person. Material collection, problem definition, and modelling approach has taken place with equal contribution from both group members.

The purpose of this report is to assess the relation between methane hydrate dissociation and future climate change. This is achieved by implementing a methane hydrate module in the Matlab model DCESS, developed by the Danish Centre for Earth System Science, and emission scenarios established by the Intergovernmental Panel on Climate Change.

We wish to thank our excellent supervisor Jens Olaf Pepke Pedersen for all guidance and inspiration throughout this project.



Ingeborg Kvalheim (s144352)



Marte Teksum Haugland (s136435)

Technical University of Denmark, DTU  
DTU Polar - National Space Institute  
Department of Environmental Engineering  
Kongens Lyngby, 16th of June, 2017

# Contents

<b>1</b>	<b>Abstract</b>	<b>1</b>
<b>2</b>	<b>Preface</b>	<b>2</b>
<b>3</b>	<b>Introduction</b>	<b>5</b>
3.1	Problem Definition . . . . .	5
<b>4</b>	<b>Theory</b>	<b>6</b>
4.1	Methane Hydrate . . . . .	6
4.1.1	Hydrate Stability Zone . . . . .	6
4.1.2	Chemical Characterization . . . . .	7
4.1.3	Geographic and Geological Setting . . . . .	10
4.2	Methane Hydrates in the Carbon Cycle . . . . .	10
4.2.1	Microbial and Thermogenic CH <sub>4</sub> Sources . . . . .	11
4.2.2	Marine, Terrestrial and Atmospheric CH <sub>4</sub> Sinks . . . . .	12
4.3	Climate Change . . . . .	14
4.3.1	Neoproterozoic (1000 – 521 Mya) . . . . .	14
4.3.2	Early Jurassic (Toarcian; 174 – 183 Mya) . . . . .	14
4.3.3	Paleocene- Eocene Thermal Maximum (55.5 Mya) . . . . .	15
4.3.4	IPCC Scenarios . . . . .	15
<b>5</b>	<b>Model</b>	<b>18</b>
5.1	DCESS Model . . . . .	18
5.2	Methane Hydrate Implementation . . . . .	20
5.2.1	Methane Hydrate Stability in Seawater . . . . .	20
5.2.2	Methane and Methane Hydrate Solubility . . . . .	21
5.3	Scenario Implementation . . . . .	22
<b>6</b>	<b>Results</b>	<b>23</b>
6.1	Dissociated Methane . . . . .	24
6.2	Atmosphere . . . . .	25
6.2.1	Temperature . . . . .	25
6.2.2	Greenhouse Gases . . . . .	27
6.3	Ocean . . . . .	29
6.3.1	Temperature, Oxygen, Methane and Nitrate . . . . .	29
6.3.2	Dissolved Inorganic Carbon and Alkalinity . . . . .	33
<b>7</b>	<b>Discussion</b>	<b>35</b>
7.1	Result Interpretation . . . . .	35
7.2	Sensitivity Analysis . . . . .	37
7.2.1	Methane Hydrate Inventory . . . . .	37
7.2.2	Release Time . . . . .	39
7.3	Comparison to Historic Hydrate Dissociation . . . . .	40
7.4	Limitations and Uncertainties . . . . .	40
<b>8</b>	<b>Conclusion</b>	<b>43</b>

<b>Appendices</b>	<b>46</b>
Appendix I: Matlab code - Methane Hydrate Implementation . . . . .	46
Appendix II: Key Variables Results . . . . .	50
A2(5°C) . . . . .	50
A2(3°C) . . . . .	51
B1(5°C) . . . . .	52
B1(3°C) . . . . .	53
Appendix III: Zero Methane Hydrate . . . . .	54
Appendix IV: Sensitivity Analysis . . . . .	55
Methane Hydrate Inventory . . . . .	55
Total Release Time . . . . .	55

### 3 Introduction

Change in Earth’s climate has been significant since the pre-industrial era. The global average surface temperature has increased with 0.85°C over the period 1880 to 2012 (IPCC, 2014). Anthropogenic influence on the climate system is clear, and greenhouse gas emissions are at their highest in modern history. Modern climate change includes widespread impacts on both human and natural systems. Snow cover and ice extent have decreased, while the global average sea level and ocean heat content have risen. Energy storage in the Earth climate system is dominated by ocean warming, which is estimated to account for more than 90 % of the energy accumulated between 1971 and 2010, while 1 % of energy was stored in the atmosphere. The observed trends and future projections of ocean temperature imply significant ocean warming over the next 100 years. Rising temperatures in the deep marine sediment, along coastal margins and in permafrost may lead to destabilization of methane hydrates, which are naturally occurring ice-like substances consisting of H<sub>2</sub>O and predominantly the gas CH<sub>4</sub> (Beaudoin et al., 2014b). As methane hydrates are stable under relatively high pressure and low temperature conditions, the climate change induced warming has the potential of accelerating the dissociation of marine methane hydrate and liberating free- and dissolved methane (CH<sub>4</sub>) gas to the sediment, water column and eventually atmosphere.

CH<sub>4</sub> has a 28-36 higher global warming potential than CO<sub>2</sub> over a 100 year period, based on its atmospheric lifetime of 12 years, energy absorbency properties and indirect effects (IPCC, 2000). The acknowledgement of CH<sub>4</sub> as a contributing factor to the sustained global warming we have experienced since the mid-twentieth century, has been affirmed (Ruppel and Kessler, 2016). Currently, CH<sub>4</sub> contributes with an equilibrium mass of 3.7 Gt C to the atmosphere. Meanwhile, previous research has estimated a CH<sub>4</sub> storage of up to 5000 Gt C in methane hydrates, although the global methane hydrate abundance is poorly understood (Ruppel and Kessler, 2016). The combination of CH<sub>4</sub> greenhouse potency and the potentially significant amounts of CH<sub>4</sub> stored in methane hydrates, has sparked research on the relationship between dissociating methane hydrates and historic climate change events. Periods of global warming in the early Palaeogene Hyperthermal events (50-57 million years ago) has been associated with pulses of carbon injected into the atmosphere. Modelling has attributed dissociating methane hydrate as potential carbon source (Ruppel and Kessler, 2016). Less emphasis has been put on current and future climate scenarios. The substantial quantities of CH<sub>4</sub> sequestered in methane hydrates and their stability in the face of sustained future global warming is an emerging field of interest in the scientific community. Improved models for assessing the methane hydrate response to future climate projections has the potential to contribute to a better understanding of the subject. In 2000, the intergovernmental Panel on Climate Change (IPCC) published four baseline greenhouse gas emission scenarios for the future (IPCC, 2000). Implementation of climate projection scenarios in Earth System Models enables research into a feasible future. The Danish Center for Earth System Science has developed the DCESS model, a comprehensive Earth System Model of low complexity and spatial resolution (Shaffer et al., 2008). It is developed for researching Earth system changes and is well suited for hypothesis testing and provides guidance for the application of more complex models.

#### 3.1 Problem Definition

The ocean module of the DCESS Earth System Model will be improved by including a detailed methane hydrate segment. Furthermore, two IPCC emission scenarios, each containing climate sensitivities of both 3°C and 5°C, are implemented. Based on the advanced DCESS model, the mission is to simulate methane hydrate dissociation as a result of future climate change and the effect dissociation will have on core elements, including temperature, atmospheric CO<sub>2</sub> and CH<sub>4</sub> concentrations and oceanic conditions.

## 4 Theory

### 4.1 Methane Hydrate

A methane hydrate is a crystalline compound in which water molecules ( $H_2O$ ) are chemically bound to  $CH_4$  or another element. The formation of methane hydrates occurs when a gas molecule reacts with water under relatively high pressure and low temperature conditions as shown in reaction 1.

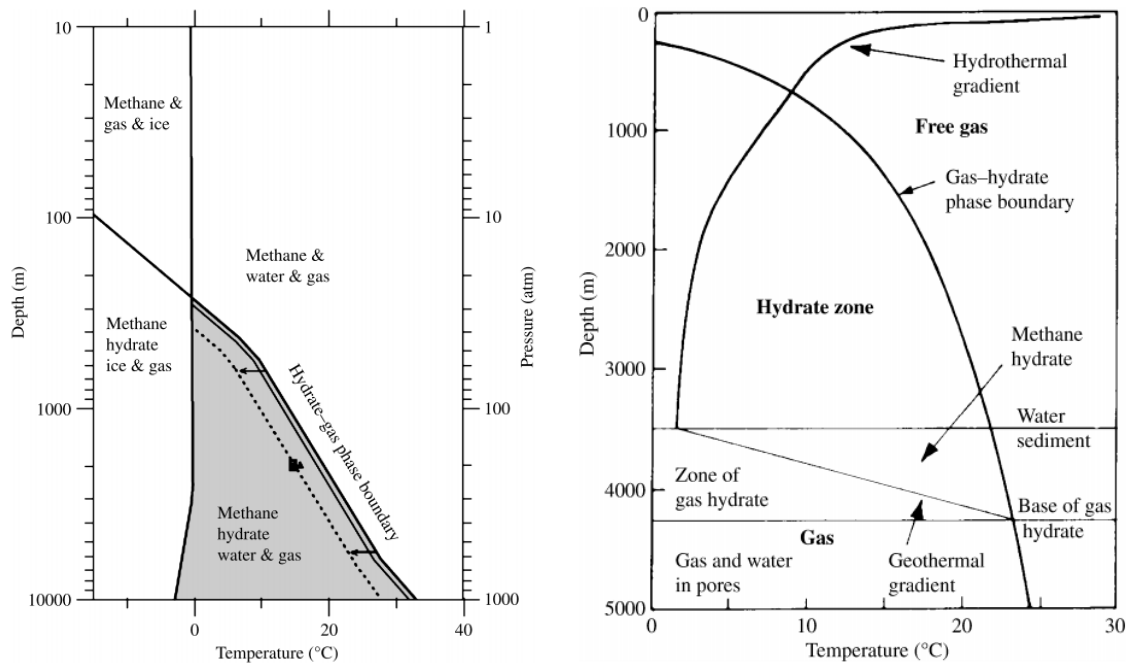


$G$  is the gas molecule and  $N_H$  is the hydration number. The methane gas molecule has a hydration number of 5.75, elaborately explained in Equation 2. One volume of saturated methane hydrate (structure I) has the storage capacity of roughly 164 volumes of gas under standardized temperature and pressure conditions. In addition to  $CH_4$ , hydrates may retain guest substances, including  $CO_2$ ,  $H_2S$  and  $N_2$  (Demirbas, 2010).

Two sources of the  $CH_4$  encapsulated in the hydrate form exist: production of  $CH_4$  situated within the hydrate stability zone and deep influx  $CH_4$ . Microbial formation of  $CH_4$  takes place both in the methane hydrate stability zone and in deeper situated sediments, while thermally formed  $CH_4$  only appears through deep influx.  $CH_4$  produced within the methane hydrate stability zone is less pure and abundant compared to deep influx  $CH_4$ . This is due to a more efficient microbial production under oxygen stressed conditions and low retention times. In addition, the sediments in the hydrate stability zone do not hold  $CH_4$  as efficiently as deeper situated sediments. Hence, the bulk amount of  $CH_4$  in hydrates originates from deep influx, where  $CH_4$  is formed below the hydrate stability zone and transported upwards by advection and dispersion. Hydrates form in the pore spaces of coarse sediments, as high permeability conditions allow  $CH_4$  to migrate to the hydrate stability zone and distribute in larger fractures, primary- and secondary pore spaces. Hence, sediment lithology determines the location of where hydrates can form. Subsequently, hydrates are often localized in highly permeable sediments as sand and volcanic ash (Beaudoin, Y.C., Dallimore, S.R., Boswell, 2014).

#### 4.1.1 Hydrate Stability Zone

Hydrate exists when the sedimentary conditions are within the hydrate stability zone, as depicted in Figure 1a. Hydrate deposit locations must fulfill conditions of low temperature and high pressure for the hydrates to be stable (Demirbas, 2010). At 1 atm pressure, methane hydrates of structure I and structure II (see Section 4.1.2) are stable at temperatures between 268.20 K and 270.20 K. This mainly occurs in permafrost and deep ocean sediments. The marine hydrate stability zone is a function of depth, geothermal gradient and seafloor temperature. Alterations of pressure and temperature affect the thickness of the stability zone. Additionally, biogeochemistry and gas abundance are contributing factors in the stability zone thickness and situation of deposits. Figure 1a illustrates the hydrate stability zone (grey) as a function of depth, temperature and pressure for pure water and pure  $CH_4$ . In addition, it illustrates the combination of physical phases under different temperature and pressure conditions. The arrows indicate the shift in hydrate-gas phase boundary under saline conditions, where the continuous line is the phase boundary for seawater and the dotted line is for brine. Notably, the stability zone has a decreasing range for increasing salinity conditions.



(a) A phase boundary diagram with the methane hydrate stability zone in grey. The depth and pressure is presented on a logarithmic scale  
 (b) Physical phase diagram of methane hydrate stability, shows the gas hydrate phase boundaries and gas hydrate zones

Figure 1: Methane hydrate stability and phase diagrams (Demirbas, 2010)

Figure 1b is a phase diagram of methane hydrate stability in a marine environment. The base of methane hydrate is the boundary between free gas and overlaying sediments where hydrates are present. The zone to the left of the gas hydrate phase boundary contains methane hydrate and free gas, while the zone to the right contains a co-existence of free gas and dissolved gas. In the sediment, there are conditions within the methane hydrate stability zone which determine the presence of hydrate. This relation depends on pressure, temperature, salinity and  $\text{CH}_4$  solubility conditions. The dissociation pressure is a function of temperature, depth and salinity. As the actual pressure exceeds the dissociation pressure and the  $\text{CH}_4$  solubility exceeds the  $\text{CH}_4$  content in hydrate form, the hydrate will dissolve and  $\text{CH}_4$  will be introduced as free- and dissolved gas in the sediment and water column.

#### 4.1.2 Chemical Characterization

A methane hydrate is an assembly of  $\text{CH}_4$  molecules that are physically bound within a crystal lattice formed by water molecules. Water molecules form hydrogen bonds with each other and are strongly polar. The water molecule structure has an angled geometry for the two hydrogen atoms from the oxygen vertex. The two lone pairs of electrons close to the oxygen is the cause of this angled effect, giving a  $104.45^\circ$  angle between the H-O-H atoms, as seen in Figure 2a. As seen in Figure 2b, the angled structure causes the water molecules to form hexagonal lattice when it freezes. A hexagonal form contains more space than the liquid space. This explains why water expands when it freezes and is therefore less dense, meaning ice will float in liquid water (Demirbas, 2010).



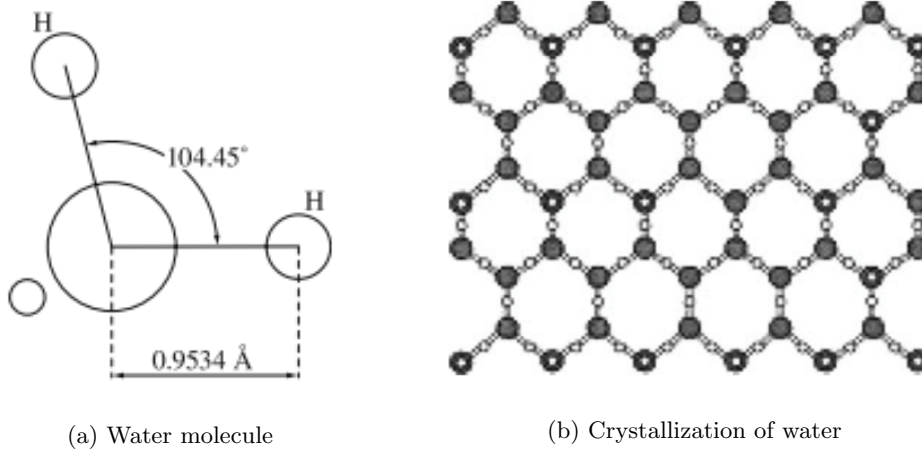


Figure 2: Structure of water (Demirbas, 2010)

Methane hydrates are formed when water freezes around the methane molecules. The host molecules ( $\text{H}_2\text{O}$ ) physically trap the guest molecule ( $\text{CH}_4$ ) while freezing, arranging themselves in a hollow polyhedral. This inclusion compound is classified as a clathrate; the cavities of the polyhedral accommodate the methane molecules without being bound to them. The stability of the clathrate hydrates is dependent on the size and shape of the gas molecule. The gas component must be small enough to fit into the cavities of the lattice and a certain fraction of the cavities must be occupied with gas molecules to ensure stability (Buffett, 2000).

A clathrate hydrate may possess many different crystal structures, but only three are known to occur naturally in the environment. The difference between these structures is determined by the amount of water molecules involved when building the crystal, which is referred as the hydration number " $N_H$ " in the generalized hydrate formula:  $\text{CH}_4 \cdot N_H \cdot \text{H}_2\text{O}$ . The hydration number ( $N_H$ ), more precisely represents the ratio between water molecules and gas molecules and the value can vary between 5.75 and 17 (Lonero, 2008). For example, the composition of a methane hydrate of structure I can be determined from Equation 2.

$$N_H = \frac{46}{2 \cdot \Theta_1 + 6 \cdot \Theta_2} \quad (2)$$

Where  $\Theta_1$  represents occupation number of small cavities and  $\Theta_2$  represents occupation number of large cavities. If  $\Theta_1$  and  $\Theta_2$  are both equal to 1, the limiting hydrate number is 5.75. structure I and structure II have both cubical structures with large and small cavity sizes, while the newly discovered structure H has a hexagonal structure and three different types of cavities. As seen in Figure 3, these structures are composed of five types of polyhedral cages: pentagonal dodecahedron ( $5^{12}$ ), tetrakaidecahedron ( $5^{12}6^2$ ), hexakaidecahedron ( $5^{12}6^4$ ), icosahedron ( $5^{12}6^8$ ) and irregular dodecahedron ( $4^35^66^3$ ). Structure I hydrates usually contain smaller guest molecules such as  $\text{CH}_4$ ,  $\text{C}_2\text{H}_6$  and  $\text{CO}_2$ , whereas structures II and H more often contain a gas mixture of larger molecules in their cavities (Liu et al., 2015).

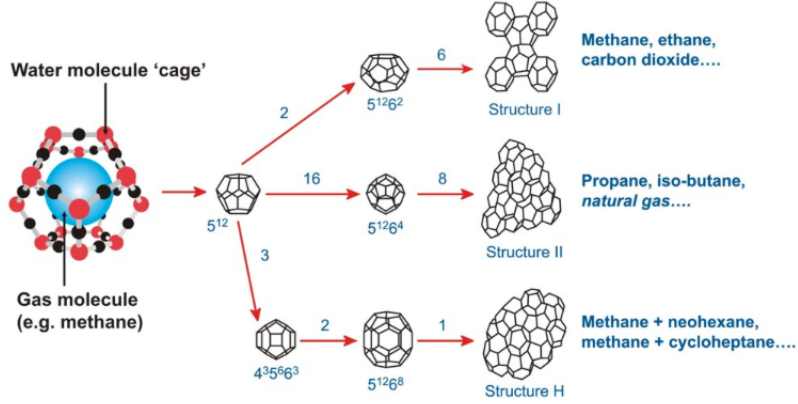


Figure 3: Hydrate structures and polyhedral cavities (Heriot Watt University, 2016)

Structure I hydrates have a  $12 \text{ \AA}$  cubic symmetry and contains 46 water molecules per unit cell where each unit cell contain two small and six large cavities with eight potential gas sites. In a small cavity, twenty water molecules are arranged to form twelve pentagonal faces, which results in a pentagonal dodecahedron ( $5^{12}$ ) cage. The twenty four water molecules in the large cavities form twelve pentagonal and two hexagonal faces, known as a tetrakaidecahedron ( $5^{12}6^2$ ) cage. Structure I has a body-centred cubic structure where the small cavities are located in the centre and the corners of the unit cell. The addition of 6 water molecules link the small cavities to form large cavities, as seen in Figure 3 (Buffett, 2000). Methane hydrates are more likely to form a structure I as the  $5^{12}$  and  $5^{12}6^2$  cages accommodate methane molecules more comfortably (Liu et al., 2015).

The unit cell of structure II contain 136 water molecules forming a  $17.3 \text{ \AA}$  cube, as seen in Figure 3. Structure II is constructed when a different arrangement of the pentagonal dodecahedron ( $5^{12}$ ) cavities create a hexakaidecahedron ( $5^{12}6^4$ ) cavity, which consists of twelve pentagonal- and four hexagonal faces. A unit cell of structure II consists of sixteen small pentagonal dodecahedron cavities and eight large hexakaidecahedron cavities with twenty four potential gas sites (Englezos, 1993). The ( $5^{12}6^4$ ) cavities form an open tetrahedral network, where their center is arranged in a manner similar to a cubic ice structure and is separated by groups of three ( $5^{12}$ ) cages. Both structure I and structure II are stabilized by a single guest gas filling at least 70% of the cavities. Gases as Ar, Kr,  $\text{O}_2$  and  $\text{N}_2$  are more likely to form structure II hydrates (Demirbas, 2010).

Structure H contains thirty four water molecules per unit cell arranged in three types of cavities with 6 potential gas sites. It consists of three pentagonal dodecahedron ( $5^{12}$ ) cavities, two irregular dodecahedron ( $4^35^66^3$ ) cavities and one icosahedron ( $5^{12}6^8$ ) cavity. A  $4^35^66^3$  cavity has three square faces, six pentagonal faces and three hexagonal faces, whereas the  $5^{12}6^8$  cavity has twelve pentagonal faces and eight hexagonal faces, as seen in Figure 3. Each of the  $5^{12}6^8$  cavity is surrounded by six  $4^35^66^3$  cavities around its central ring of six hexagons. The ( $5^{12}6^8$ ) cavities form columns by joining their top and bottom hexagonal faces (Demirbas, 2010). Both  $5^{12}$  and  $4^35^66^3$  are small cavities and can accommodate small gas molecules supporting the structure, whereas the large  $5^{12}6^8$  cavity can accommodate even larger gas molecules, such as butane ( $\text{C}_4\text{H}_{10}$ ) (Khokhar et al., 1998).

### 4.1.3 Geographic and Geological Setting

Methane hydrates primarily exist in two domains: high latitudes and along continental margins in the oceans. This is due to the prerequisite pressure and temperature relations of the hydrate stability zone, accompanied by the requirement of large quantities of organic matter for bacterial methanogenesis to take place. Most hydrates exist at continental margins, where the rates of organic carbon burial and primary production are large. Approximately 90 % of organic carbon is presently found under shallow waters near the continental shelves (Demirbas, 2010). Hydrates form under conditions of high pressure and low temperature, making two locations appropriate: in the Arctic and Antarctic permafrost and below the ocean surface at depths greater than 300 meters (Beaudoin et al., 2014a). The reservoirs are often associated with reservoirs of other hydrocarbons, such as oil and natural gas. Figure 4 illustrates the global occurrence of methane hydrates, detected seismically or by well logging.

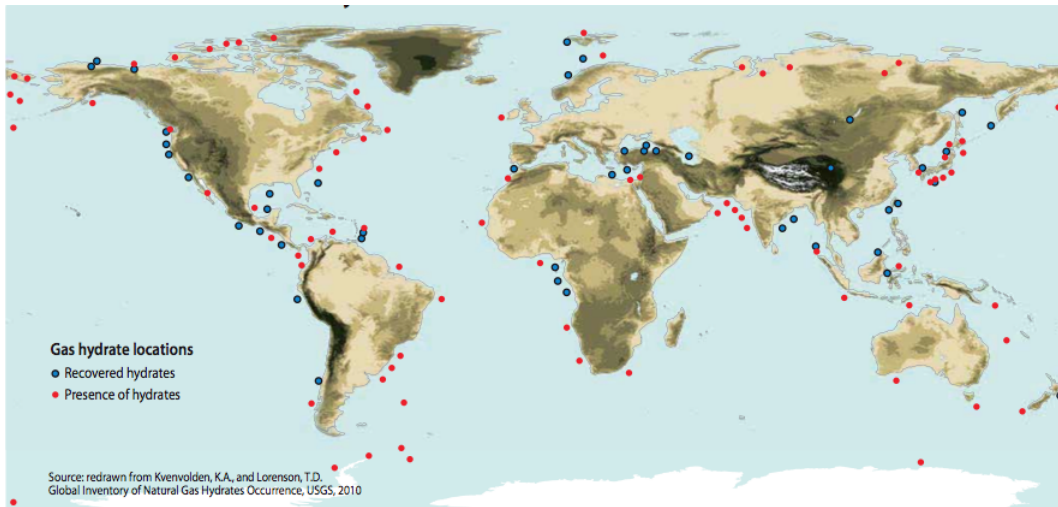


Figure 4: Locations of recovered (blue) and present (red) methane hydrates (Demirbas, 2010)

Host sediments determine the form of which methane hydrates appear. Hydrates predominantly exist in unconsolidated sand or clay. The silt and sand sediments have a porosity and permeability of 30-45 % and 500-200 md, respectively, without methane hydrate embedded. With methane hydrate, the porosity decreases to 10-15 % and permeability to 0.1-0.5 md at a gas saturation between 50-90 %. In clay rich sediments without methane hydrate, the porosity ranges between 50-70 % and the initially low permeability decreases with depth. With hydrate present in the small pores between grains, the porosity is decreased to 45-60 % and the permeability is lower than 0.0001 md, virtually zero (Beaudoin, Y.C., Dallimore, S.R., Boswell, 2014).

## 4.2 Methane Hydrates in the Carbon Cycle

The methane production-, transformation- and transportation processes' significance in global carbon cycles, is presently deficient and must be researched (Beaudoin et al., 2014a). Hydrate bound  $\text{CH}_4$  in deep marine sediments plays a dynamic role in the carbon cycling between the atmosphere, hydrosphere, geosphere and biosphere. With respect to the objectives of this thesis, the sinks described are with regards to the dissociation of methane hydrate and the corresponding migration

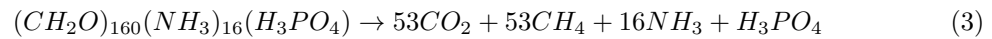
of the released  $\text{CH}_4$ . The sources described are the origins of the  $\text{CH}_4$  bound in hydrate. Presently there is a global, relative equilibrium between sources and sinks of methane from hydrates, although local variations do exist (Archer, 2007). Table 1 sums up abundance, sources and sinks for  $\text{CH}_4$  related to hydrates in different geological settings.

Table 1: Overview of suggested abundance, sources and sinks in the main methane hydrate settings (Ruppel and Kessler, 2016)

Setting	$\text{CH}_4$ (Gt C)	Source	Sink
Deep marine	1717	Microbial	Seafloor: AOM, permeability, Water column: MOx, bubble stripping
Upper continental slope	63	Microbial	Seafloor: AOM, permeability, Water column: MOx, bubble stripping
Subglacial	80-400	Microbial Thermogenic	Onshore: anaerobic/aerobic processes in sediments Seafloor: AOM Water column: MOx, bubble stripping
Subsea permafrost	-	Thermogenic	Seafloor: AOM Water column: MOx, bubble stripping
Onshore permafrost	20	Thermogenic	Permeability, ice blocked migration pathways, anaerobic/aerobic processes

#### 4.2.1 Microbial and Thermogenic $\text{CH}_4$ Sources

Microbial formation of  $\text{CH}_4$  is the main contributing factor in Earth's sub-seabed  $\text{CH}_4$  concentrations. Additionally, thermal production from organic carbon generates hydrocarbon liquids and gases;  $\text{CH}_4$  being one of them. Methanogens produce  $\text{CH}_4$  as a derivative of their degradation of organic materials in suboxic and anoxic locations where the organic carbon levels are high. It is derived that hydrate production is a function of sedimentation rates and primary productivity of organic carbon, temperature and pressure (Beaudoin et al., 2014a). In the microbial process, organic debris is decomposed to  $\text{CH}_4$  in an anoxic environment. Carbon-, hydrogen- and phosphorous-containing organic material in the ratio 106:16:1 is decomposed by the following reaction:



Acetate fermentation and  $\text{CO}_2$  reduction are also a stage in the decomposition which produces  $\text{CH}_4$ , presented respectively in the reactions:



and



In addition to microbial formation, thermal  $CH_4$  production generally occurs on extensive depth, more than 2000 meters, in sediment layers at more than 273 K temperature.  $CH_4$  production occurs by thermal degradation of oil in petroleum areas and maturation of coal, and is one of the resulting hydrocarbons (Beaudoin et al., 2014b).

#### 4.2.2 Marine, Terrestrial and Atmospheric $CH_4$ Sinks

$CH_4$  can be dissociated from hydrates. When addressing physical, chemical and biological sinks of methane released from hydrates, there are four main environments to consider: anoxic sediments, oxygenated sediments, the water column and the atmosphere. Atmospheric  $CH_4$  concentrations originating from hydrates are low, as the sinks are strong (Ruppel and Kessler, 2016). Figure 5 sums up the sinks of  $CH_4$  from the point of methane hydrate dissociation in the sediments to the atmosphere.

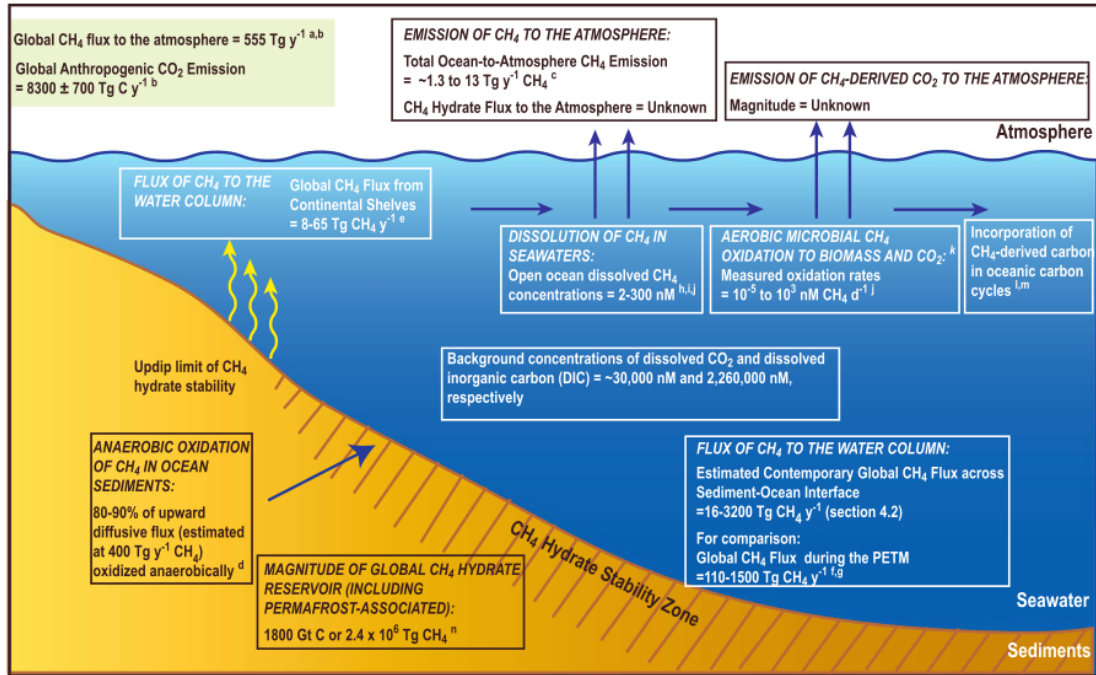
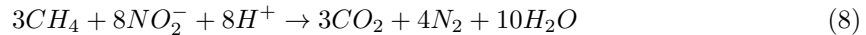
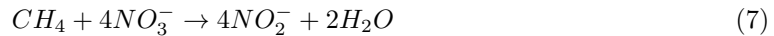
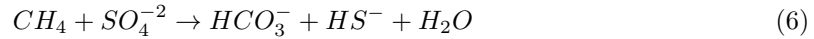


Figure 5: Sinks of  $CH_4$  released from methane hydrates (Ruppel and Kessler, 2016)

The first sink after  $CH_4$  release occurs in the marine sediments. In anoxic sediments the primary sink of methane, anaerobic oxidation of methane (AOM), occurs. The anaerobic microorganisms methanotrophic archaea and sulphate-reducing bacteria enable  $CH_4$  to oxidize with varying electron acceptors as sulphate (abundant in seawater), nitrate, nitrite and metals, and hereby creating a biofilter that prevents  $CH_4$  from migrating up to the sea floor. Local variations are observed, and a high methane flux makes AOM less efficient, and ascending gas may avoid the biofilter. This indicates that the AOM area is thin when the vertical methane flux is high and vice versa. The amount of methane absconding is dependent on the flux magnitude. Typical areas where AOM does not occur are fault zones or mud volcanoes, where sulphate is prevented from entering the

sediments as a consequence of the substantial methane flux. Between 80 % and 90 % of the 400 Tg/yr upward flux of  $\text{CH}_4$  is consumed by the AOM process (Ruppel and Kessler, 2016). Equation 6 describes the overall reaction coupled to sulphate reduction, while Equation 7 And Equation 8 are the overall reactions of AOM coupled to nitrate and nitrite reduction.



As seen in Equation 6, the AOM sulphate reaction produces bicarbonate ( $\text{HCO}_3^-$ ), which subsequently increases the alkalinity. The resulting carbonate precipitation contributes to additional removal of carbon in the carbon cycle. Isotopic characterization of carbonates indicates if the carbon is a derivative of destabilized methane hydrates. Lastly in the sediment section, the physical properties of the sediments are affecting the released  $\text{CH}_4$ s ability to migrate to the water column. Low permeability, saturation and stalemate cavities decelerate the advection process and result in a delay in the upward flux of  $\text{CH}_4$  (Beaudoin et al., 2014b).

The  $\text{CH}_4$  bypassing the sedimentary sinks will reach the water column and its associated sinks. Here, two governing processes counteract further  $\text{CH}_4$  migration to the atmosphere. Because the overall  $\text{CH}_4$  concentration in oceans is low, considerable amounts of the gas present in bubbles will diffuse, despite  $\text{CH}_4$ s low solubility in saline water.  $\text{CH}_4$  is substituted by oxygen and nitrogen, which also have low solubilities, in this bubble stripping process.  $\text{CH}_4$  released from the seafloor will be dissolved deep in the water column. Once dissolved,  $\text{CH}_4$  in shallow waters can be emitted to the atmosphere by gas exchange while deeper located  $\text{CH}_4$  can persist in the ocean for centuries, dependent on ocean circulation conditions below the ocean-atmosphere mixing layer. Aerobic microbial oxidation (MOx) takes place in the presence of dissolved  $\text{CH}_4$  and  $\text{O}_2$ . Several studies have concluded that the rate of oxidation increases with increasing  $\text{CH}_4$  concentrations (Crespo-Medina et al., 2014).  $\text{CH}_4$  is the main energy source and structural carbon source for methanotrophic bacteria, and oxidized  $\text{CH}_4$  is transformed to bacterial biomass and dissolved inorganic carbon (DIC).  $\text{CH}_4$  and  $\text{O}_2$  are biologically and chemically converted to  $\text{CO}_2$ . Bubble stripping and aerobic microbial oxidation (MOx) prevent the entering of  $\text{CH}_4$  to the atmosphere, but may impact ocean chemistry and biodiversity. Extensive oxidation might lead to deoxygenation of the water and chemical depletion. It may also increase the ocean pH and consequently lead to ocean acidification, as the  $\text{CO}_2$  production and concentration increases (Beaudoin et al., 2014b).

Terrestrial sinks are relevant when addressing  $\text{CH}_4$  released from methane hydrates located in permafrost. As the magnitude of this reservoir is estimated to approximately 1% of the global methane hydrate inventory, it is not elaborately explained. The sulphate amounts in terrestrial sediments are lower than in oceanic sediments, hence, the oxidation process is deemed of a lower magnitude in the terrestrial segment. Similarly to ocean sediments, permeability and geological trap structures may function as a sink, in symbiosis with ice filling the pore spaces, which is also inhibiting the upward flux of  $\text{CH}_4$ . In the atmosphere, an estimated amount of 90% of the released  $\text{CH}_4$  is removed by oxidation with the hydroxyl radical within the 12-year atmospheric lifetime of  $\text{CH}_4$ . The net reaction of the  $\text{CH}_4$  oxidation mechanism results in the production of  $\text{CO}_2$  in the troposphere and ozone depleting  $\text{H}_2\text{O}$  in the stratosphere, both potent greenhouse gases (Ruppel and Kessler, 2016).

### 4.3 Climate Change

Historically, the  $\text{CH}_4$  level in the atmosphere have been higher in interglacial periods than glacial periods, and dissociation of methane hydrates during deglaciation has been linked to the end of glacial periods (Kretschmer et al., 2015). In glacial periods, formation of ice from sea water causes a fall in sea level and subsequent depressurization of methane hydrates. This initiates the warming of the atmosphere. Furthermore, in interglacial periods, a positive feedback process occurs as the highly potent greenhouse gas  $\text{CH}_4$  from methane hydrates is released to the atmosphere. With sufficient temperature increase of the deep oceans, methane hydrates will destabilize and release sufficient  $\text{CH}_4$  to the atmosphere to accelerate temperature increase. On the other hand, a rise in sea level is a negative feedback, as sufficient pressure increase induces hydrate stabilization and inhibit release of  $\text{CH}_4$ . Other effects of dissociating hydrates are massive sedimentary landslides as a result of decreased seafloor stability, as well as ocean anoxia and acidification leading to changes in the distribution and diversity of mainly marine biota. In historical climate minimums and maximums, methane hydrates have been hypothesized as an important contributor to climate change.

#### 4.3.1 Neoproterozoic (1000 – 521 Mya)

The Neoproterozoic is the terminal period of the Proterozoic Eon and is subdivided into the Tonian, Cryogenian and Ediacaran period. This was a period affected by two extreme glaciations, and in the later part of the era, the Ediacaran period, the earliest evidence of multicelled life. The severe glaciation occurred during the Cryogenian period, when ice sheets reached the equator and there is reason to believe that the oceans were almost entirely frozen, which formed a possible “Snowball Earth”. The Neoproterozoic is punctuated by two glaciations – The Stuartian at 720 Mya and the Marinoan at 635 Mya. Stuartian marks the return of glaciation to Earth after billion years absence (Pierrehumbert et al., 2011).

Authigenic cap carbonates occurring in thin layers (up to 5 meters thick), are overlying the siliciclastic glacial sediments deposited in coherence with these global cooling events. There are found cap carbonates with similar texture and features to those produced by contemporary  $\text{CH}_4$  cold seep processes and with a strong negative  $\delta^{13}\text{C}$  carbon excursion.  $\delta^{13}\text{C}$  carbon describes an isotopic signature reflecting the ratio between the stable isotopes:  $^{13}\text{C}/^{12}\text{C}$ . This indicates that a large reservoir of light  $\delta^{13}\text{C}$   $\text{CH}_4$  have been released and oxidized during the formation of the carbonates. The hypothesis around these observations is dissociation of methane hydrates in terrestrial permafrost, sub sea permafrost hydrates and most of the marine methane hydrates, during deglacial events. It is estimated that a  $\text{CH}_4$  release of 3000 Gt C may have occurred from non-marine methane hydrates during warming following the Marinoan deglaciation. The deglaciation event is postulated to have set the stage for the biogeochemical changes necessary for the explosion of life in the Cambrian era (Ruppel and Kessler, 2016).

#### 4.3.2 Early Jurassic (Toarcian; 174 – 183 Mya)

A strong negative  $\delta^{13}\text{C}$  carbon-isotope excursion of - 5 ‰ to - 7 ‰ indicates the occurrence of a disturbance in the global carbon cycle during the Early Jurassic period. Astronomical changes superimposed on long term global warming have been hypothesized to have triggered the release of isotopically light carbon. Rapid release of  $\text{CH}_4$  as a result of methane hydrate dissociation at the continental shelf, has been put forward as a possible explanation for injection 5000 Gt C to the ocean-atmosphere system. The carbon isotope signature is larger than the one associated with at the end of Neoproterozoic and the one characterized during the Paleocene-Eocene Thermal Maxi-

num. Ocean anoxia and other ocean geochemical changes, coincided with the inferred dissociation event, which affected the strength of the water column  $\text{CH}_4$  sink. The  $\text{CH}_4$  release is associated with widespread extinction of marine species (Ruppel and Kessler, 2016).

#### 4.3.3 Paleocene- Eocene Thermal Maximum (55.5 Mya)

The Paleocene Eocene Thermal Maximum (PETM) was a hyperthermal event leading to a  $6^\circ\text{C}$  increase in the global temperature. This includes a temperature rise of  $4\text{--}5^\circ\text{C}$  in low latitude and  $6\text{--}8^\circ\text{C}$  in high latitude, within 10 000 to 30 000 years (Higgins and Schrag, 2006). The abrupt negative carbon isotope excursion and extreme global warmth during the PETM have been linked to a massive dissociation of sedimentary methane hydrate. Isotopic records indicate that deep ocean temperature increased with more than  $4^\circ\text{C}$ , together with  $3.5\text{‰}$  to  $5\text{‰}$  negative excursion in the marine  $\delta^{13}\text{C}$  carbon (R. Dickens et al., 1995). The methane hydrate hypothesis state that the source of the PETM carbon isotope excursion was the release of 1100 to 2100 Gt dissociated  $\text{CH}_4$  from hydrate (Ruppel and Kessler, 2016). The triggering mechanism for the release remains uncertain. However, the magnitude of warming and rise of the carbonate compensation depth indicates that the amount of observed carbon addition was larger than the methane hydrate hypothesis could account for. It is found that oxidation of at least 5000 Gt C organic carbon is the most likely explanation for the geochemical and climatic changes observed during the PETM. The large- scale release of  $\text{CH}_4$  from continental margins requires sufficient quantity of global methane hydrate reservoir. Constant supply of  $\text{CH}_4$  is needed for stabilization of the hydrate in marine sediments due to diffusion and advection (Higgins and Schrag, 2006). Another quandary is that the isotopic excursion is consistently larger in terrestrial records than in deep ocean sediment cores, which may have a poorer preservation of the event. If a marine source is in relation to the carbon isotopic anomaly, then the marked change in terrestrial carbon isotopes during PETM indicates that water column oxidation sink did not prevent  $\text{CH}_4$  carbon emissions to the atmosphere. Recent studies constrained the release rate of carbon during the PETM to  $< 1.1 \text{ Pg yr}^{-1}$  compared to the current rate range from 0.016 to  $3.2 \text{ Pg yr}^{-1}$ , which indicates that the modern seafloor  $\text{CH}_4$  emissions is comparable to that during the PETM. Recent modeling provides the possibility that multiple carbon ( $\text{CH}_4$  and/or  $\text{CO}_2$ ) emission events and possible multiple sources may be required to explain the observational data for the PETM (Ruppel and Kessler, 2016).

#### 4.3.4 IPCC Scenarios

The intergovernmental Panel on Climate Change (IPCC) have developed long term emission scenarios to analyze the possible climate change, its impacts and options to mitigate climate change. Emissions of greenhouse gases in the future is a very complex system, determined by different driving forces such as demographic development, socio-economic development, and technological change. The evolution of the emissions is very uncertain and different scenarios are therefore alternatives to how the future might unfold and how driving forces may influence them. The scenarios assist in climate change analysis, thereby climate modelling and the assessment of impacts, adaption and mitigation. The possibility that any of the emission paths described in the scenarios will occur, is related to a high uncertainty (IPCC, 2000).



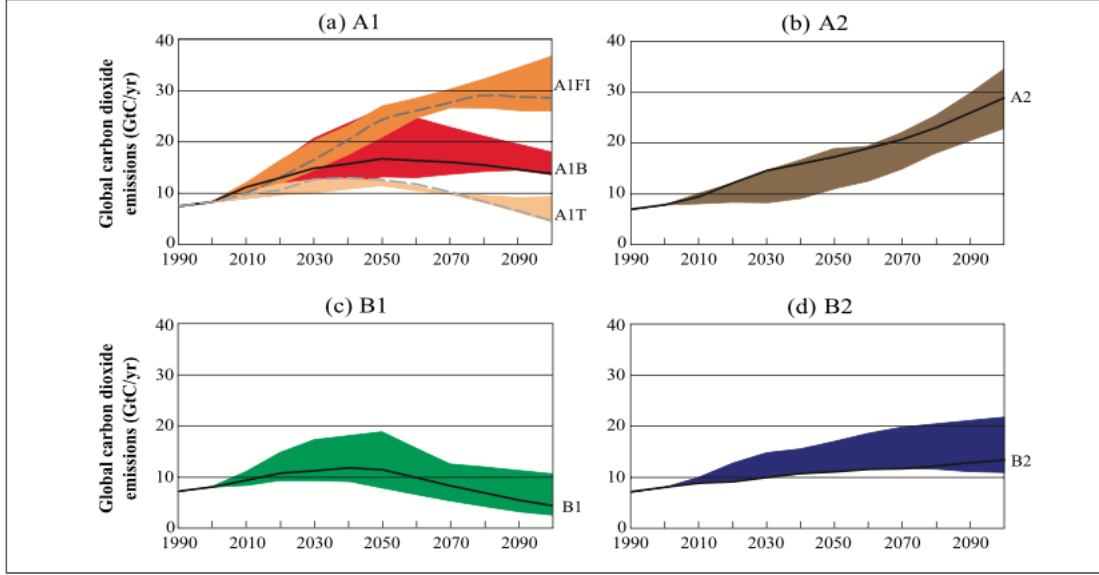


Figure 6: The four IPCC climate change scenarios: A1, A2, B1 and B2. The graphs show the predicted development in atmospheric CO<sub>2</sub> emissions from 1990 to 2100. The A1 scenario has three sub scenarios, illustrated in transparent orange, red and orange. The remaining three scenarios have only one path. The width of the colored field indicates the range of uncertainty (IPCC, 2000)

Figure 6 shows four different storylines, A1, A2, B1 and B2, developed to describe the relationship between emission driving force and their evolution. The diversity of these scenarios is amplified by high economic growth and different treatment of technology. The four families shown in Figure 6, consist of six scenario groups within them. Scenarios A2, B1 and B2 all have one group each, while A1 have three groups within the family (IPCC, 2000). As seen in Figure 6, the A2 and B1 storylines are representing both worst and best case scenarios, respectively. These scenarios are therefore implemented in the DCESS Earth system model to simulate future climate change, and are further given a more extensive scenario description.

The A2 storyline is characterized by low trade flows, relatively slow capital stock turnover, and slow technological progress. The scenario builds on large self-reliance in terms of resources and less emphasis on economic, social and cultural interactions between regions. A A2 world has less international cooperation compared to the A1 and B1 scenarios, which affect people, ideas and capital to be less mobile and technology to diffuse slowly. The storyline emphasizes family and community life, which affect the fertility rates to decline relatively slowly. The A2 scenario has the largest population of 15 billion people by 2100. Some regions experience a technological change that is more rapid than average, while other experience slower. This is caused by industry adjustments to local resource endowment, as well as cultural and educational levels. Regions with access to large energy and mineral resources develop more resource-intensive economies. Regions with poor access to resources will try to improve resource efficiency by minimizing import dependency through technological innovation. The use of fuel is different between regions, depending on resource availability. Regions with high income, but are resource-poor will evolve towards advanced post-fossil technologies, as renewable and nuclear, while regions with low-income, but are resource-rich will rely on traditional fossil technologies. The main focus for innovation and development, as well as an environmental concern, is agricultural productivity as the large population leads to a substantial food requirement. There is a greater emphasis on potential local and regional

environmental damage, while global environmental concern are relatively weak (IPCC, 2000).

The B1 storyline builds on the characteristics of a high level of environmental and social consciousness together with global measures to obtain a more sustainable development. Governments, businesses, media and the public place environmental and social aspects of development on the agenda. The storyline describes a rapidly changing and convergent world, where a large part of its gain is invested in improved efficiency of resource use, equity, social institutions and environmental protection. Diffusion of cleaner technologies is an important effort to increase resource efficiency and achieve the goals of sustainability. Both organizational and technical change entails high levels of material and energy saving in the way of maximizing reuse and recycling to reduce material wastage, and at the same time a reduction in pollution. As in A1, there is a low mortality and fertility rate, motivated partly by social and environmental concerns. The global population increases to 9 billion in 2050 and declines thereafter to 7 billion by 2100. The B1 world has high levels of economic activity with a deliberate progress toward international and national income equality. There is spent more on quality rather than quantity, as there is an emphasis on less material goods and increased prices on resources caused by environmental taxation. As the conventional oil and gas resources decline, energy systems will transition into post-fossil technologies driven by environmental concerns. The high environmental consciousness leads to high environmental quality at a local, national and international level. Examples of this are transboundary air pollution and land use, where activities potentially damaging to the environment are counteracted, cities are designed for public and non-motorized transport, and a strong motivation for low-impact agriculture, as well as maintenance of large areas of wilderness, which contribute to high food prices, but also a lower level of meat consumption. These environmental measures and policies leads to relatively low greenhouse gas emissions, even without explicit interventions to mitigate climate change. (IPCC, 2000).

## 5 Model

### 5.1 DCESS Model

The Danish Center for Earth System Science (DCESS) – has designed a Earth System Model to simulate global change in large time scale and features atmosphere, ocean, ocean sediment, land biosphere and lithosphere components. The model can be used to explore how the Earth system functioned in the past and how it might behave in the future, thereby also in response to anthropogenic forcing scenarios. The geometry consists of one hemisphere divided at 52° latitude, into two 360° wide zones, the low-mid latitude and high latitude sectors. By doubling the hemisphere values, the global reservoirs and fluxes are obtained. The low-mid- and high latitude sectors divide the Earth surface by the proportion 84:16, respectively. The ocean module covers 70.5 % of the Earth surface, is 270° wide and extends from the equator to 70° latitude as illustrated in Figure 7. The ocean is divided into 55 layers with 100 meter vertical resolution to maximum depths of 5500 meter for each sector. The 55 ocean layers are each assigned an ocean sediment section with widths representing modern day hypsography. CH<sub>4</sub> cycling has been implemented in the model and deals with both aerobic, suboxic and anoxic conditions, radiative forcing and CH<sub>4</sub> lifetimes relevant for high atmospheric CH<sub>4</sub> concentrations. An extensive set of simulations has been carried out for CH<sub>4</sub> inputs of various sizes, time scale and ocean-atmosphere partitions to review model behaviour (Shaffer et al., 2008).

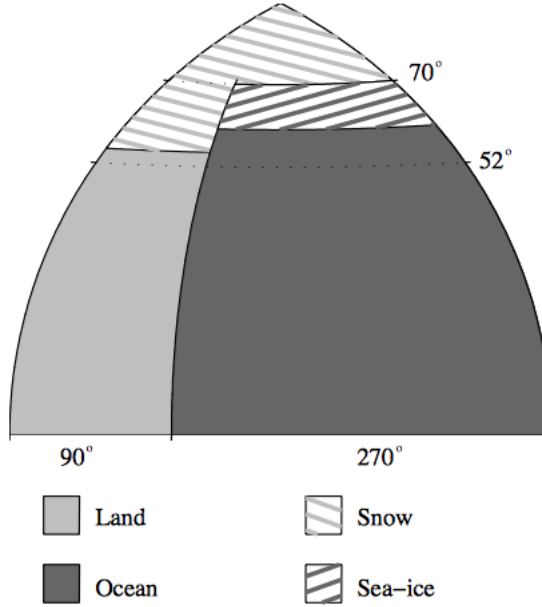


Figure 7: DCESS model configuration containing land, ocean, snow and sea-ice components. The model consist of one hemisphere dividing low-mid latitude and high latitude into 360° wide sectors at 52 °latitude. The ocean model extends from the equator to 70 °latitude and is 270° wide, dividing the low-mid latitude and high latitude ocean sectors into the ratio 84:16, respectively. The ocean model covers 70.5 % of the model surface (Shaffer et al., 2008).

The atmosphere module includes radiation balance, meridional transport of heat and water vapor between low-mid- and high latitude zones, and heat and gas exchange with the ice-free part of the ocean. The relevant gases are CO<sub>2</sub> and CH<sub>4</sub> for three carbon isotopes (C<sup>12</sup>, C<sup>13</sup> and C<sup>14</sup>), nitrous oxide and oxygen. Atmospheric CH<sub>4</sub> will dominantly oxidize to CO<sub>2</sub> by reaction with the OH radical. By this reaction, the concentration of the OH radicals will be depleted and CH<sub>4</sub> atmospheric lifetime,  $\tau$ , grows as CH<sub>4</sub> concentrations increase. This effect together with the associated chemical reactions in the troposphere and stratosphere, is addressed by Equation 9.

$$\tau = \tau_{PI}(M + b)/[(1 - a)M + b] \quad (9)$$

$\tau_{PI}$  is the pre-industrial (PI) lifetime,  $a$  and  $b$  are fitting constants and  $M$  equals  $(pCH_4 - pCH_{4,PI})/pCH_{4,PI}$ , where  $pCH_4$  is the partial pressure of CH<sub>4</sub>.

The ocean module considers tracers as temperature, salinity, oxygen isotopes in water, phosphate, dissolved oxygen, dissolved inorganic carbon for all three carbon isotopes and alkalinity, and has a prescribed circulation and mixing. Significant oxidation of  $\text{CH}_4$  in the ocean interior will induce suboxic and anoxic ocean conditions. To deal with this, the model includes nitrogen and sulphur cycling with the ocean tracers of nitrate ( $\text{NO}_3$ ), ammonium ( $\text{NH}_4$ ) and hydrogen sulphide ( $\text{H}_2\text{S}$ ). The following processes are the most important related to massive injection of  $\text{CH}_4$  in ocean nitrogen and sulphur chemistry. A generalization of new production of organic matter in the surface layer has been made to depend on limiting nutrients, either phosphate or nitrate, which gives Equation 10.

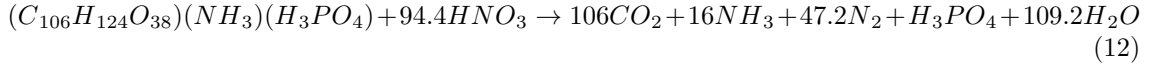
$$NP^{l,h} = \min(NPP^{l,h}, NPN^{l,h}) \quad (10)$$

$NPP^{l,h}$ ,  $NPN^{l,h}$  refer to the new production of phosphate and nitrate in the low-mid and high latitude ocean zones (l,h), and is given by Equation 11.

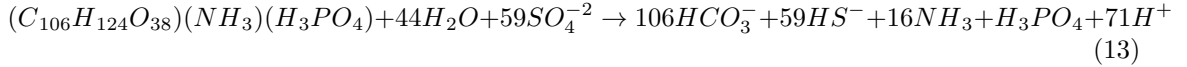
$$A_0^{l,hni} z_{\text{eu}} (1, r_{\text{NP}})^{-1} (L_f^{l,h} / \text{sy}) (PO_4^{l,h}, NO_3^{l,h}) [PO_4^{l,h} / (PO_4^{l,h} + P_{1/2})], [NO_3^{l,h} / (NO_3^{l,h} + N_{1/2})] \quad (11)$$

$A_0^{l,hni}$  refers to the ice-free ocean surface area,  $z_{\text{eu}}$  is the surface layer depth,  $r_{\text{NP}}$  is the Red-field ratio,  $L_f^{l,h}$  are efficiency factors, sy is the number of seconds per year,  $PO_4^{l,h}$  and  $NO_3^{l,h}$  are phosphate and nitrate concentrations in surface layer,  $P_{1/2}$  and  $N_{1/2}$  are half saturation constants.

Remineralization will occur through oxidation of organic matter with dissolved oxygen, if oxygen is above a certain minimum level  $O_{2,\text{min}}$ . Below this oxygen level, will remineralization occur through denitrification as long as nitrate exceed a certain minimum  $NO_{3,\text{min}}$ . The oxidation equation for denitrification is given as:



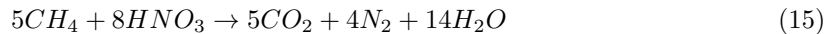
When the oxygen and nitrate concentration are below their minimum levels, remineralization is assumed to occur in the way of sulphate reduction. The sulphate dependent oxidation equation is given by:



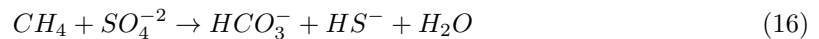
Both denitrification and sulphate reduction produces ammonia which has a minor contribution to an increased alkalinity. However, sulphate reduction also contributes to alkalinity decrease because production of hydrogen ion exceeds the alkalinity increase from production of bisulfide. Ammonia and bisulfide, produced by denitrification and sulphate reduction, are oxidized to nitrate and sulphate. This occur when transported by advection and diffusion to oxygenated ocean layers, where  $O_2 \geq O_{2,\text{min}}$ .  $\text{CH}_4$  in the ocean module is acted upon by advection, diffusion, air-sea gas exchange and microbial oxidation in the water column.  $\text{CH}_4$  oxidation in oxygenated ocean layers ( $O_{2,n}^{l,h} \geq O_{2,\text{min}}$ ), consumes oxygen and produces  $\text{CO}_2$ , as expressed by:



Nitrate dependent, microbial AMO (anoxic  $\text{CH}_4$  oxidation) reaction are characterized by  $O_2 < O_{2,\text{min}}$  and  $NO_3 > NO_{3,\text{min}}$  for suboxic/weakly anoxic conditions, and is expressed as:



sulphate dependant, microbial AMO reaction for anoxic conditions are characterized by  $O_2 < O_{2,\text{min}}$  and  $NO_3 < NO_{3,\text{min}}$  and expressed as:



The production of bicarbonate and bisulphide in sulphate dependant AMO, leads to a strong alkalinity decrease. An increase in ocean alkalinity will depress dissolved  $\text{CO}_2$  concentrations in the ocean and in the atmosphere. Lastly, there is an air-sea gas exchange for  $\text{CH}_4$ , dependant on gas transfer velocity,  $\text{CH}_4$  solubility and the dissolved  $\text{CH}_4$  concentration in the ocean surface layers.

## 5.2 Methane Hydrate Implementation

The ocean module of the current DCESS (version 1.2) model handles methane hydrate with a predetermined total amount of release of thermogenic  $\text{CH}_4$  from hydrates. The initial release timepoint is defined by the user. In addition, a user-determined fraction of the total  $\text{CH}_4$  is defined to be released within a certain time frame after initial release time. This indicates that as long as the time point is higher than the initial release time, there will be a uniform release of  $\text{CH}_4$  from hydrates to all 55 ocean layers. Part of the implementations in this project is to introduce a higher resolution of detail in the DCESS ocean hydrate module. Therefore, an initial amount of  $\text{CH}_4$  is set to exist in hydrate form. The amount is uniformly distributed in ocean layers estimated to contain hydrates between 400 and 1400 meters. The main focus of the improvement of the methane hydrate segment of the program has been to implement  $\text{CH}_4$  solubility within the GHSZ with a basis in the approach of Tishchenko et. al (Tishchenko et al., 2005). Thermodynamic equations for the stability and solubility of methane hydrate in seawater are established and added to the program, enabling a more accurate estimation of the behaviour of methane hydrate in terms of stability and solubility as a function of pressure, temperature and salinity. See Appendix I for the detailed AtmMet\_M.m matlab code.

### 5.2.1 Methane Hydrate Stability in Seawater

Equation 17 is the fundamental equation in calculation of hydrate stability, finding the pressure at which methane hydrate starts dissolving ( $P_{dis}$ ). The pressure at which methane hydrates dissociate ( $P_{dis}$ ) has been calculated for temperature ranges from 273-293 K and salinity ranges from 0-70.

$$\begin{aligned} \ln(P_{dis}) = & \ln(\phi_{CH_4}^* \cdot P_{dis}^* / \phi_{CH_4}) + \frac{V_H \cdot (P_{dis} - P_{dis}^*)}{RT} \\ & + \frac{n \cdot [V_w^* \cdot (P_{dis}^* - P^o) - \bar{V}_w \cdot (P_{dis} - P^o)]}{RT} \\ & + n \cdot \left[ -\ln(a_w^{sw})^{P^o} + \frac{m_{CH_4} - m_{CH_4}^* \cdot S \cdot k_{set} - m_{CH_4} \cdot \ln(1 - 0.00100511 \cdot S)}{m_w} \right] \end{aligned} \quad (17)$$

where  $\phi_{CH_4}$  is the fugacity coefficient of  $\text{CH}_4$  in vapour phase,  $V_H$  is the molar volumetric properities of hydrate, while  $V_w^*$  and  $\bar{V}_w$  are molar volumetric properties of respectively pure water and water.  $P^o$  is the standard state pressure of 0.1 MPa. R is the gas constant, T is temperature, S is salinity, n is the hydration number, and  $k_{set}$  is the Setschenow coefficient. The expression  $-\ln(a_w^{sw})$  is the water activity of sea water.  $m_{CH_4}$  and  $m_w$  are the molalities of respectively  $\text{CH}_4$  and water. The superscript notation \* corresponds to pure water while the superscript notation sw indicates sea water.

An iterative procedure conducted by Tishchenko et. al including Equation 17 and equations for partial molar volume of water in sea water, molality of  $\text{CH}_4$ , dissociation pressure of hydrate in pure water and solubility of  $\text{CH}_4$  in sea water, allowed the calculation of  $P_{dis}$  of methane hydrate as a function of temperature and salinity. The resulting empirical solution of Equation 17 is presented in Equation 18, a solution with 0.009 MPa standard deviation. Figure 8 illustrates the calculated dissociation pressure for hydrates in seawater for a range of salinities.

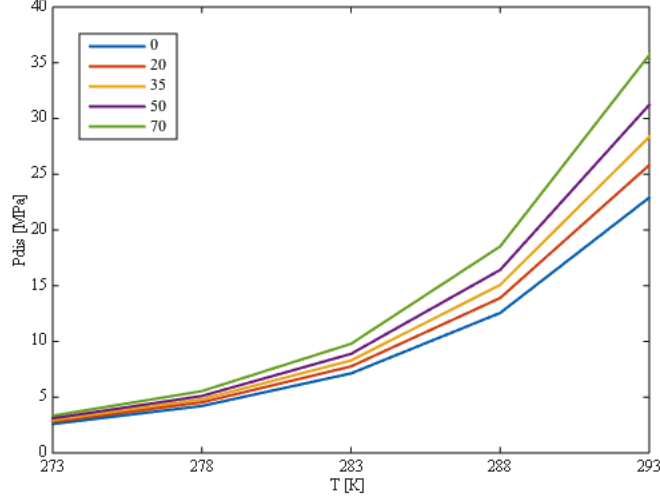


Figure 8: Dissociation pressure [MPa] for salinities of 0, 20, 35, 50 and 70. The disassociation pressure of methane hydrate is increasing with increasing salinity, with a higher difference at higher temperatures.

$$\begin{aligned}
\ln(P_{dis}^{sw}) = & -1.6444866 \cdot 10^3 - 0.1374178 \cdot T + 5.4979866 \cdot 10^4 / T + 2.64118188 \cdot 10^2 \cdot \ln(T) \\
& + S \cdot [1.1178266 \cdot 10^4 + 7.67420344 \cdot T - 4.51521310^{-3} \cdot T^2 - 2.04872879 \\
& \cdot 10^5 / T - 2.17246046 \cdot 10^3 \cdot \ln(T)] + S^2 \cdot [1.70484431 \cdot 10^2 + 0.118594073 \cdot T \\
& - 7.0581304 \cdot 10^{-5} \cdot T^2 - 3.09796169 \cdot 10^3 / T - 33.2031996 \cdot \ln(T)]
\end{aligned} \tag{18}$$

### 5.2.2 Methane and Methane Hydrate Solubility

The solubilities of  $\text{CH}_4$  and methane hydrates in seawater have been calculated with a basis in  $P_{dis}$ , for temperature and salinity ranges of respectively 273-290 K and 0-70. Equation 19 describes the natural logarithm of methane hydrates for the three coexisting phases:  $\text{CH}_4$  gas,  $\text{CH}_4$  hydrate and seawater.

$$\begin{aligned}
\ln(C_{CH_4})_{P_{dis}^{sw}} = & -2.5640213 \cdot 10^5 - 1.6448053 \cdot 10^2 \cdot T + 9.1089042 \cdot 10^{-2} \cdot T^2 + 4.90352929 \\
& \cdot 10^6 / T + 4.93009113 \cdot 10^4 \cdot \ln(T) + S \cdot [-5.16285134 \cdot 10^2 - 0.33622376 \cdot T \\
& + 1.88199047 \cdot 10^{-4} \cdot T^2 + 9.76525718 \cdot 10^3 / T + 9.9523354 \cdot 10^1 \cdot \ln(T)]
\end{aligned} \tag{19}$$

Equation 20 is the empirical solution for  $\text{CH}_4$  solubility, calculated for temperature ranges between 273-293 K and salinities from 0-70. It addresses the solubility of  $\text{CH}_4$  at any condition of coexistence in the  $\text{CH}_4$  gas phase and the  $\text{CH}_4$  hydrate phase.

$$\begin{aligned}
\ln(C_{CH_4})_{sw} = & \ln(C_{CH_4})_{P_{dis}^{sw}} + [5.04597 \cdot 10^{-2} + 7.64415 \cdot 10^{-4} \cdot S \\
& - (3.90236 \cdot 10^{-4} + 5.48947 \cdot 10^{-6} \cdot S) \cdot T + (7.06154 \cdot 10^{-7} + 9.87742 \\
& \cdot 10^{-9} \cdot A) \cdot T^2] \cdot (P - P_{dis}) + [7.57285 \cdot 10^{-5} - 1.90867 \cdot 10^{-8} \cdot S \\
& - 1.4483 \cdot 10^{-10} \cdot S^2 - (1.96207 \cdot 10^{-7} - 6.67456 \cdot 10^{-11} \cdot S) \cdot T] \cdot (P - P_{dis})^2
\end{aligned} \tag{20}$$

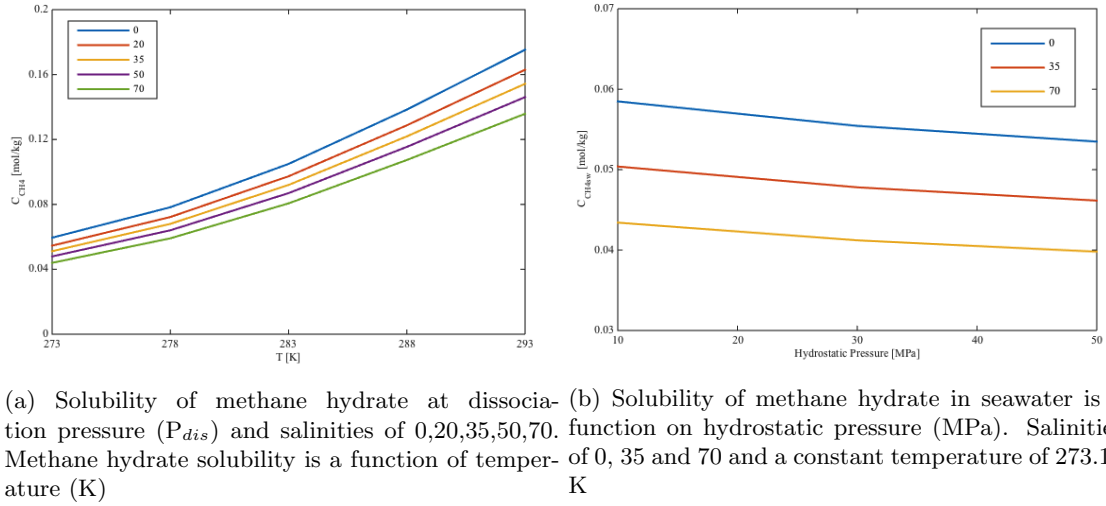


Figure 9: Solubility of methane hydrate ( $C_{CH_4}$ ) in mol/kg.

Figure 9a represents the temperature dependency of  $CH_4$  hydrate solubility while Figure 9b illustrates the pressure dependency of  $CH_4$  hydrate solubility in seawater at a temperature of 273.15 K and at a range of salinity conditions.

### 5.3 Scenario Implementation

Forcing-files are collected from a previous DCESS model, containing forcing for future scenarios and climate sensitivities. The model focuses on the A2 scenario and B1 scenario, created by the IPCC, where each scenario have climate sensitivities of both 3°C and 5°C. The forcing contains calculations of  $CO_2$  release, aerosol forcing and  $CH_4$  release prior to year 2100 AD, with different parameters as inputs. In Table 2 the most central control parameters to the calculations, related to scenario and sensitivity, are presented.

Table 2: Scenario control parameters for after the year 2100 (LWR = long wave radiation)

	A2 3°C	A2 5°C	B1 3°C	B1 5°C
Outgoing LWR (W/m <sup>2</sup> )	211.13	218.91	211.13	218.91
LWR sensitivity (W/m <sup>2</sup> /K)	1.93	1.37	1.93	1.37
Total $CO_2$ (ppm)	962.7	962.7	147.3	147.3
Total Aerosol (W/m <sup>2</sup> )	-18.85	-17.92	-19.76	-15.36
Total $CH_4$ (Gt C)	20.692	20.692	4.83	4.83

## 6 Results

Two scenarios with two climate sensitivities have been simulated, resulting in four separate output results (A2(5°C), A2(3°C), B1(5°C) and B1(3°C)). The presented data are the results of a 500 year period run, from 1750, representing the pre-industrial era, until the end year 2250. The result presented are temperature and atmospheric greenhouse gas changes with time. Furthermore, ocean depth profile curves describing temperature, CH<sub>4</sub> concentration, O<sub>2</sub>, nitrate, alkalinity and dissolved inorganic carbon as a function of depth are presented for further analysis.

Table 3: Chosen values for input parameters in the methane hydrate module simulation

	A2(3°C)	A2(5°C)	B1(3°C)	B1(5°C)
<b>CH<sub>4tot</sub> (Gt C)</b>	63	63	63	63
<b>RT<sub>HL</sub> (yr)</b>	90	90	90	90
<b>RT<sub>LL</sub> (yr)</b>	90	90	90	90
<b>Hydrate Depth<sub>HL</sub> (m)</b>	400-1400	400-1400	400-1400	400-1400
<b>Hydrate Depth<sub>LL</sub> (m)</b>	800-1400	800-1400	800-1400	800-1400

In the methane hydrate segment, certain input parameters are set by the user. These include the total CH<sub>4</sub> inventory existing in layers (CH<sub>4tot</sub>), total release time (RT) and determination of the layers containing CH<sub>4</sub>. Table 3 sums up the chosen parameters used in the following result presentation. The underscores HL and LL represent high latitude and low latitude. CH<sub>4tot</sub> is based on (Ruppel and Kessler, 2016), which estimates a 63 Gt C CH<sub>4</sub> inventory in upper continental slopes. Upper continental slopes are estimated to have a high sensitivity to climate change. The depths containing CH<sub>4</sub> are therefore set to correspond to upper continental slope depths, the interval between 400 meters and 1400 meters. Results with CH<sub>4tot</sub> set to estimates of the total global inventory (e.g. 1800 Gt C (Ruppel and Kessler, 2016)) can be utilized distributed from upper continental slope and down to deep marine settings (ca. 400 meters to 5500 meters) with an output corresponding to the results based on solely upper continental slope inventory. The total release time after dissociation is set to 90 years, but is uncertain and therefore analyzed in detail in Section 7.2, which also entails a sensitivity analysis of the inventory magnitude (CH<sub>4tot</sub>).

In Appendix II, plots of new production, O<sub>2</sub>,  $\delta^{18}\text{O}$ ,  $\delta^{13}\text{C}$ , land biosphere carbon, carbonate compensation depth (CCD), organic carbon burial and sedimentation velocity for each scenario can be found.



## 6.1 Dissociated Methane

Figure 10 illustrates the net released  $\text{CH}_4$  from dissociated hydrate into the ocean sediment. All four combinations of scenario and sensitivity are included. The red bar represents low latitude  $\text{CH}_4$  release and the blue bar portrays high latitude  $\text{CH}_4$  release. In Appendix II, the detailed  $\text{CH}_4$  release to low latitude and high latitude ocean layers as a function of time and depth is included.

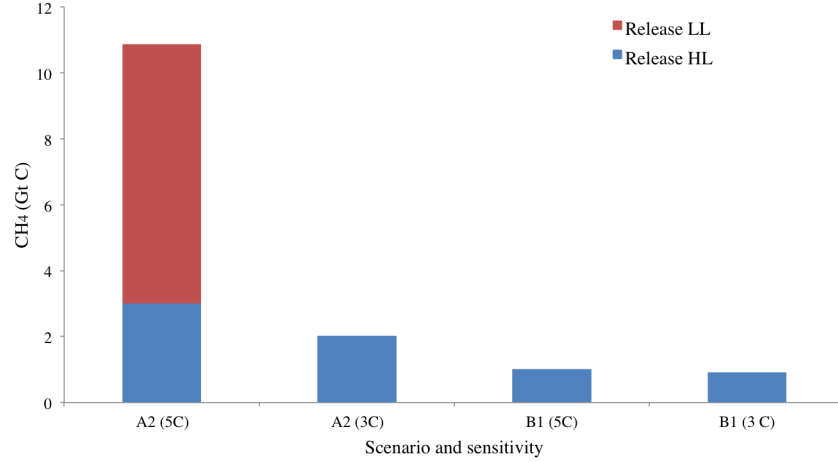


Figure 10: Total release of  $\text{CH}_4$  with a 500 year simulation from 1750 to 2250, in association with latitude, scenarios and sensitivities.

The most prominent net release is observed in the A2(5°C) scenario. The first destabilized hydrates are found at 400 meters depth in high latitudes at simulation year 2040. Moreover, the methane hydrate inventory of the three layers down to 700 meters depth dissociates and releases  $\text{CH}_4$  prior to 2150. The total high latitude release is of 3.0 Gt C. The most substantial contribution to the total release however, occurs in low latitudes, as 84 % of the total  $\text{CH}_4$  inventory is assumed to be located here, and each layer therefore contains more  $\text{CH}_4$ . In 2180, instability occurs at 800 meters depth in low latitudes. The total low latitude release is of 7.8 Gt C. 17 % of the 63 Gt C inventory is released in total in the A2(5°C) scenario. In the A2(3°C) scenario, two pulses of the high latitude hydrates are dissociating. This occurs in 2050 at 400 meters depth, a offset of 10 years compared to the A2(5°C) scenarios initial release time. The second pulse of  $\text{CH}_4$  is released at 500 meters depth in 2130. Of the total methane hydrate inventory, 3.2 % is released over the 500 year period. In the B1(5°C) scenario, the only release occurs at 400 meters depth in year 2040. 1.6 % of the total inventory is released. Lastly, the B1(3°C) scenario has a high latitude release 20 years later than the B1(5°C) scenario. The release occurs at 400 meters depth in year 2060. In B1(3°C), which is the weakest forcing scenario, 1.4 % of the total inventory of 63 Gt C is released before 2250. High latitude hydrates are more sensitive to temperature change in the ocean and moreover prone to destabilization. A cascade reaction is observed as the most shallowly located hydrates destabilize first. An initial release in a shallow layer introduces a positive system feedback and deeper located hydrates destabilize as a result of this feedback and programmed warming contributions from the respective scenario.

## 6.2 Atmosphere

For more detail regarding the following Section, Appendix II includes endpoint variable values for other relevant atmospheric tracers.

### 6.2.1 Temperature

The initial, pre-industrial atmospheric temperature for all scenarios is 20.9°C in low latitudes and -4.3°C in high latitudes, while the ocean surface temperature commences at 21.7°C in low latitudes and 0.4°C in high latitudes. Common for all four scenario and sensitivity combinations is that the temperature curve slope steepens after year 2000 and levels off after 2100, a direct effect of the IPCC scenario initiation in early 2000 and attainment of maximum duration in 2100. With the presence of a protracted scenario extending beyond the year 2100, the temperature would certainly keep increasing after 2100.

Figure 11, 12, 13, and 14 have analogous layouts with red lines representing low latitude temperature, blue lines representing high latitude temperature and the dotted line representing the weighted average temperature as a function of time. As 84 % of the model area belongs to the low latitude zone and 16 % to the high latitude zone, the average global temperature curve is closer to the low latitude values. The A1 scenario inflicts a higher impact on temperature advancement than the B1 scenario. The temperature stabilizes after year 2100, as the scenario effect ends.

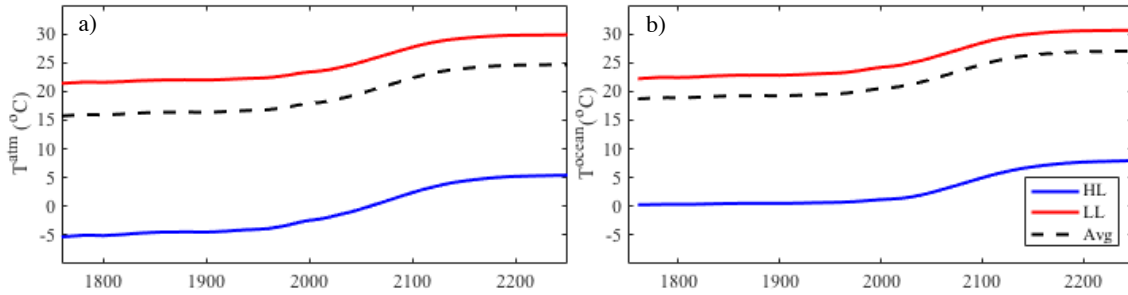


Figure 11: Scenario A2 with 5 °C climate sensitivity. (a) Atmospheric temperature as a function of time. (b) Ocean surface temperature as a function of time.

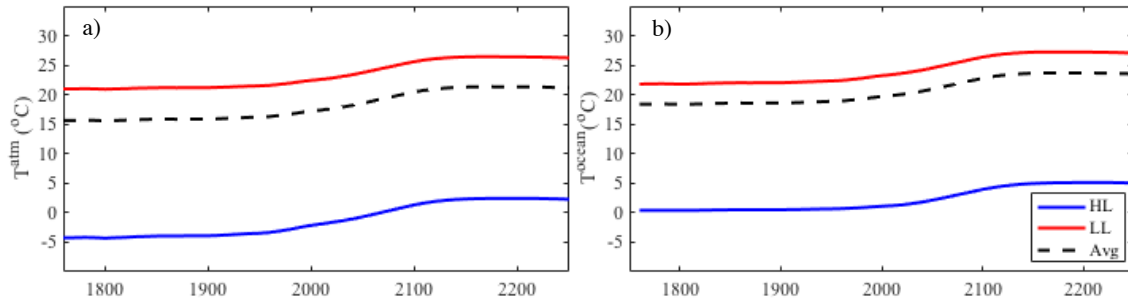


Figure 12: Scenario A2 with 3 °C climate sensitivity. (a) Atmospheric temperature as a function of time. (b) Ocean surface temperature as a function of time.

Figure 11 and Figure 12 illustrate the change in atmospheric (a) and surface ocean (b) temperature in the A2 scenario with climate sensitivities of respectively 5°C and 3°C. In Figure 11a there is a 8.9°C atmospheric temperature increase in low latitude and 9.8°C temperature increase in high latitude over the 500 year time span. In Figure 12a, representing the 3°C climate sensitivity, the increase is less prominent, with 5.2°C in low latitudes and 6.5°C in high latitudes. Figure 11b illustrates the 8.9 and 7.6°C temperature increase in ocean temperatures for low latitudes and high latitudes at sensitivity of 5°C. In Figure 12b, representing the 3°C sensitivity scenario, the ocean surface temperature increase is of 5.2°C in low latitudes and 4.5°C in high latitudes. Conclusively, the tendency in the A2 scenario is that the net atmospheric temperature increase is most sizeable in the high latitude segment. Reversely, the ocean temperature change has its greatest range in low latitudes when comparing high and low latitude temperature responses to climate change.

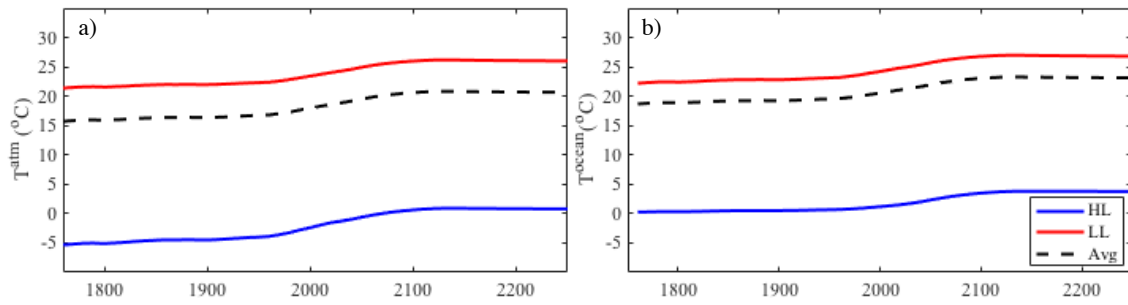


Figure 13: Scenario B1 with 5°C climate sensitivity. (a) Atmospheric temperature as a function of time. (b) Ocean surface temperature as a function of time.

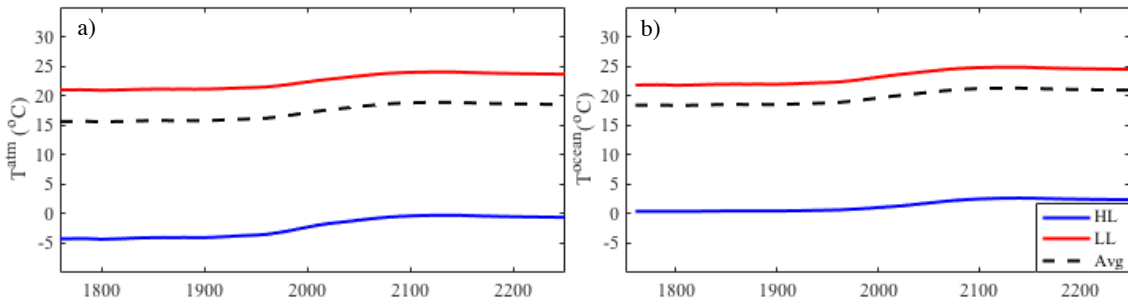


Figure 14: Scenario B1 with 3°C climate sensitivity. (a) Atmospheric temperature as a function of time. (b) Ocean surface temperature as a function of time.

Figure 13a and 14a represent the atmospheric temperature development under the B1 scenario, with a sensitivity of 5°C in Figure 13a and a sensitivity of 3°C in Figure 14a. For the 5°C sensitivity, both the low latitude and high latitude temperatures increase with 5.0°C. In the 3°C sensitivity scenario, the low latitude and high latitude atmospheric temperatures increase with respectively 2.7°C and 3.7°C. The surface ocean temperature in Figure 13b indicates a high latitude temperature change of 3.4°C and a low latitude temperature increase of 5.0°C under 5°C sensitivity conditions. Figure 14b involves a temperature increase with 2°C in high latitudes and 2.7°C in low latitudes. In correspondence to the A2 scenario, the B1 scenario also proves the largest atmospheric temperature increase in high latitudes and the largest surface ocean temperature increase in low latitudes.

## 6.2.2 Greenhouse Gases

The initial pre-industrial, atmospheric gas concentration are given for low latitude as it represents 84 % of the atmosphere. The start concentrations are equal for all scenarios, where the  $\text{CO}_2$  concentration is  $290 \mu\text{atm}$ ,  $\text{CH}_4$  concentration is  $1.05 \mu\text{atm}$  and  $\text{N}_2\text{O}$  is given to  $2.8 \mu\text{atm}$ . In all scenarios, the  $\text{CH}_4$  concentration reaches its maximum around year 2100, and declines thereafter. This is due to a limitation in the scenario parameters, as the emissions are only modelled until the year 2100. With a prolonged scenario beyond year 2100, the  $\text{CH}_4$  concentration would be expected to keep increasing.

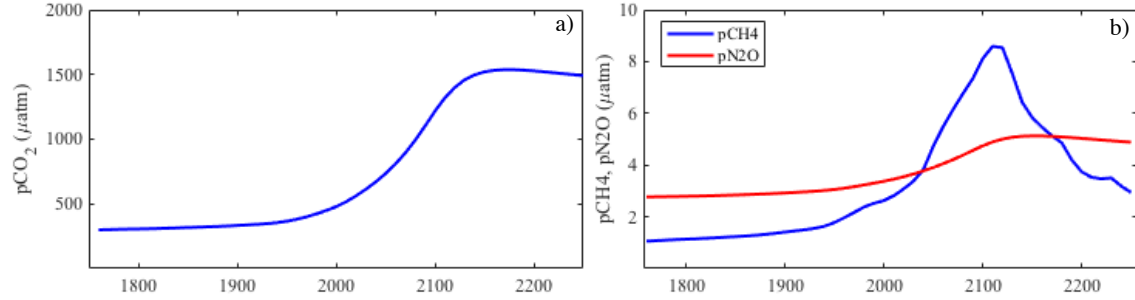


Figure 15: A2 scenario with  $5^\circ\text{C}$  sensitivity (a) Atmospheric  $\text{CO}_2$  concentration (b) Atmospheric  $\text{CH}_4$  and  $\text{N}_2\text{O}$  concentration

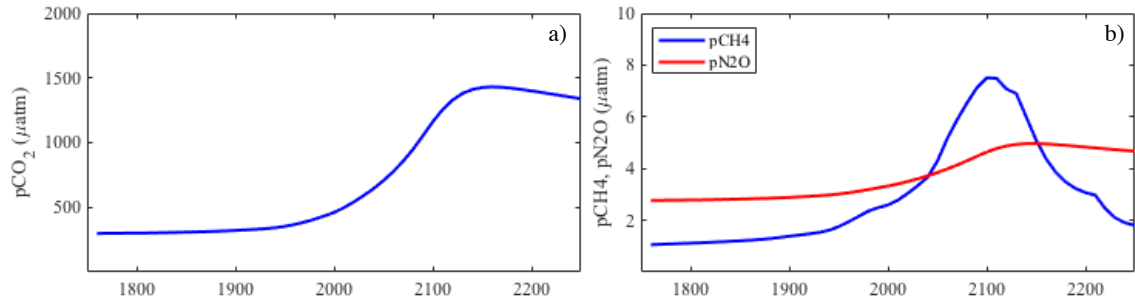


Figure 16: A2 scenario with  $3^\circ\text{C}$  sensitivity (a) Atmospheric  $\text{CO}_2$  concentration (b) Atmospheric  $\text{CH}_4$  and  $\text{N}_2\text{O}$  concentration

Figure 15 and 16 illustrate the atmospheric gas concentrations, predicted in the A2 scenario from year 1750 to 2250 with a climate sensitivity of  $5^\circ\text{C}$  and  $3^\circ\text{C}$ . The  $\text{CO}_2$  concentration from 1750 to 2000 is at a stable level of around  $290 \mu\text{atm}$ , with few variations for both sensitivities. Around year 2000, the concentration start to increase drastically and reaches its maximum concentration of  $1500 \mu\text{atm}$  in Figure 15a and  $1400 \mu\text{atm}$  in Figure 16a, in 2150. The  $\text{CO}_2$  concentrations is thereafter starting to decline.

The  $\text{N}_2\text{O}$  concentration curve has equal variations in both sensitivities, with a stable concentration around the initial value of  $2.8 \mu\text{atm}$  until year 2000, whereas the concentration start to increase. It reaches its maximum concentration of  $4.5 \mu\text{atm}$  in 2130, and thereafter starts to gently decrease. Figure 15b and 16b illustrate similar variations of  $\text{CH}_4$  concentrations, from 1750 until it reaches year 2100. Figure 15b reaches a maximum  $\text{CH}_4$  concentration of  $8.6 \mu\text{atm}$  in 2100, while 16b reaches a maximum of  $7.5 \mu\text{atm}$  in 2100. The maximum concentrations is impacted by the

scenario as well as a  $\text{CH}_4$  release in high latitude layers at year 2050. Thereafter, the concentrations are declining in both sensitivities. The  $\text{CH}_4$  concentration in Figure 15b are decreasing more rapidly from 2100 until 2150 than from year 2150 to 2250. The  $5^\circ\text{C}$  sensitivity has a release in high latitude layers in 2040, 2100 and 2150, and in low latitude layers in 2180. The low latitude release is illustrated as a small incline in the curve at year 2180, before it declines again. The curve in  $3^\circ\text{C}$  is decreasing more gently from 2100 to 2130, than from 2130 to 2220, which is explained by the release of  $\text{CH}_4$  in high latitude layers at year 2130.

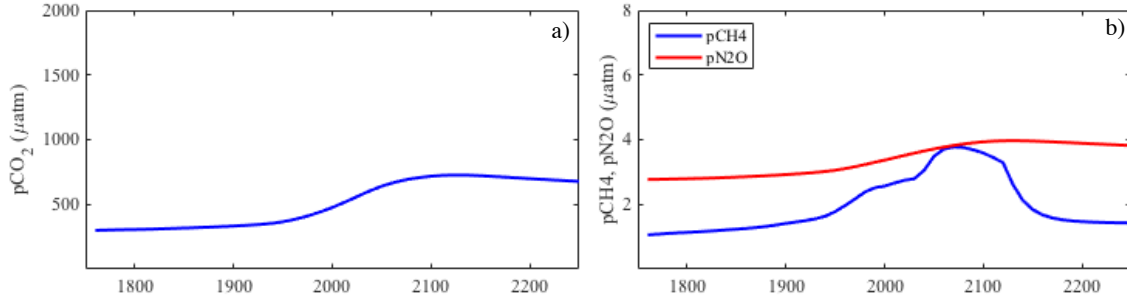


Figure 17: B1 scenario with  $5^\circ\text{C}$  sensitivity (a) Atmospheric  $\text{CO}_2$  concentration (b) Atmospheric  $\text{CH}_4$  and  $\text{N}_2\text{O}$  concentration

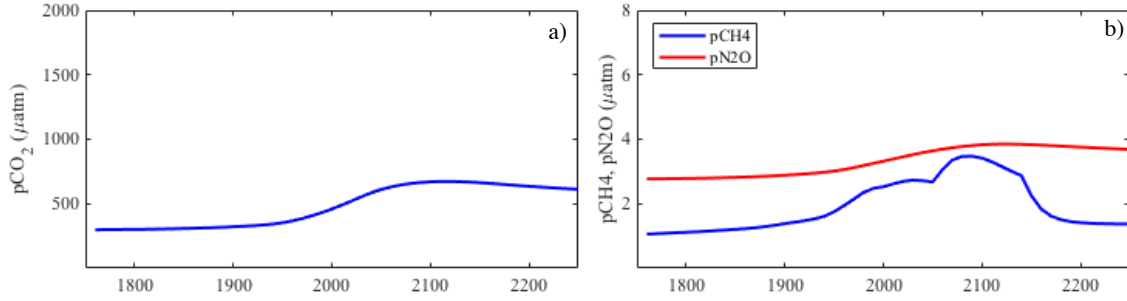


Figure 18: B1 scenario with  $3^\circ\text{C}$  sensitivity (a) Atmospheric  $\text{CO}_2$  concentration (b) Atmospheric  $\text{CH}_4$  and  $\text{N}_2\text{O}$  concentration

Figure 17 and 18 present the atmospheric gas concentrations predicted in the B1 scenario from year 1750 to 2250, with a climate sensitivity of  $5^\circ\text{C}$  and  $3^\circ\text{C}$ . The  $\text{CO}_2$  concentrations in Figure 17a and 18a show little variation until year 2000, where the concentration start increasing. The difference between the sensitivities is seen in the final value at year 2250. Figure 17a shows a final value of 680  $\mu\text{atm}$ , while Figure 18a has a final value of 610  $\mu\text{atm}$ . The  $\text{CO}_2$  concentrations show a maximum value at year 2100 for both sensitivities, where the concentration reaches 700  $\mu\text{atm}$  at  $5^\circ\text{C}$  sensitivity, and 650  $\mu\text{atm}$  at  $3^\circ\text{C}$  sensitivity.

The  $\text{N}_2\text{O}$  concentration curve illustrates little variation until year 2000, where it starts to increase. Both sensitivities reach a maximum concentration of 4  $\mu\text{atm}$  at year 2100, where it thereafter starts gently to decrease. There is a minimal difference in the end concentration, as seen in Figure 17b and 18b. The  $5^\circ\text{C}$  sensitivity has an end concentration of 3.8  $\mu\text{atm}$ , while the  $3^\circ\text{C}$  sensitivity has an end concentration of 3.7  $\mu\text{atm}$ . There is a difference in the  $\text{CH}_4$  concentration curve in the time interval between 2000 and 2100, as seen in Figure 17b and 18b. Both sensitivities have release of  $\text{CH}_4$  in high latitude during this period of time, but with difference in the year

the release is initiated. For 5°C sensitivity, the layer starts releasing CH<sub>4</sub> in 2040, while it for 3°C sensitivity starts releasing in 2060. This explains the variations in the incline of the curve, before they both reach maximum concentrations in year 2100. Figure 17b shows a maximum concentration of 3.8  $\mu\text{atm}$ , while Figure 18b shows a maximum concentration of 3.6  $\mu\text{atm}$ . The CH<sub>4</sub> concentrations start decreasing with comparable slopes after 2100, as no more CH<sub>4</sub> is released.

## 6.3 Ocean

In this section, the results presented are depth profiles extracted from timepoints in the simulation where CH<sub>4</sub> has been released from dissociating hydrates. In Appendix II, the behaviour of more oceanic parameters are included.

### 6.3.1 Temperature, Oxygen, Methane and Nitrate

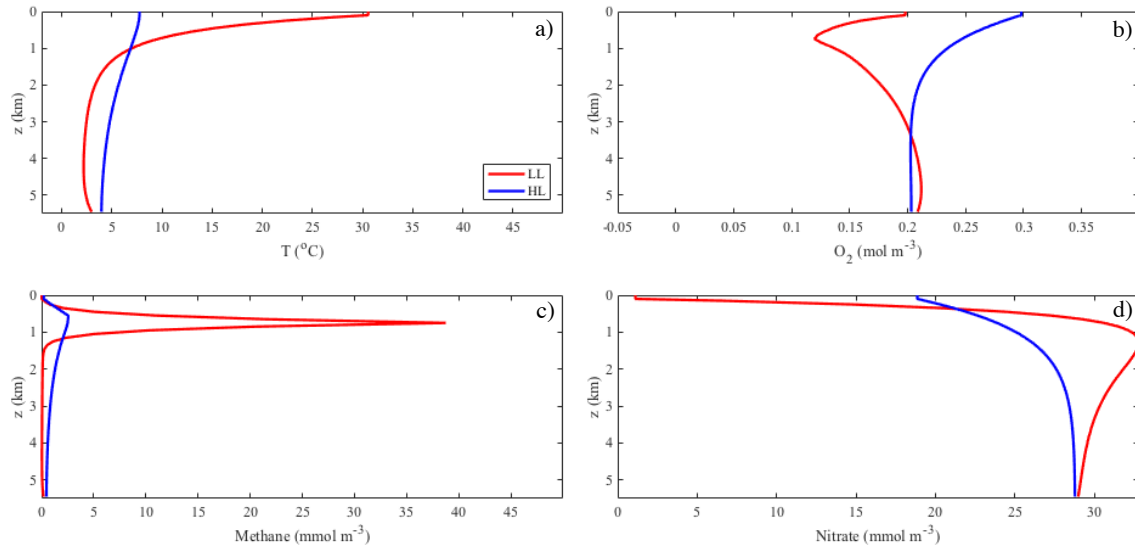


Figure 19: Depth profiles for scenario A2 with 5°C climate sensitivity for high latitude and low latitude ocean at simulation year 2200. (a) Temperature, (b) O<sub>2</sub>, (c) CH<sub>4</sub> concentration and (d) Nitrate concentration

The temperature ocean profile at year 2200 of the A2 (5°C) simulation (Figure 19a, shows a relatively stable temperature profile in high latitudes, decreasing from 6°C at the surface to 4°C in the deep marine setting. In low latitudes, the thermocline is at its most prominent from 300 meters depth to 1500 meters depth. In shallow waters the temperature is stable around 30°C, and when the thermocline ends, the temperature is stabilizing at 2.5°C, before a slight increase at 5000 meters depth to 3°C.

Figure 19b is the O<sub>2</sub> concentration profile. At the surface, the O<sub>2</sub> concentration of high latitudes is at 0.3 mol/m<sup>3</sup>, while low latitudes has 0.2 mol/m<sup>3</sup>. Both latitudes have a corresponding oxygen loss of 0.08 mol/m<sup>3</sup> down to 700 meters depth. Subsequently, the low latitude curve increases until 5000 meters depth, where the concentration is stabilizing at 0.21 mol/m<sup>3</sup>. Conclusively, there is an oxygen consumption down to 700 meters depth. The high latitude profile decreases down to 2000 meters depth, whereas it stabilizes at 0.21 mol/m<sup>3</sup>.

Figure 19c shows the  $\text{CH}_4$  concentration profile in year 2200. The concentration is peaking at 500 meters depth in high latitudes and at 800 meters depth in low latitudes. This is a result of dissociating methane hydrates. High latitudes dissociation starts at 400 meters depth in year 2040, and at 500 meters depth in 2100 and at 600 meters depth in 2150. In low latitudes, dissociation starts in 2180 at 800 meters depth. The methane hydrate concentration in low latitudes is  $39 \text{ mmol/m}^3$  while the high latitude concentration is at  $2.5 \text{ mmol/m}^3$ . The maximum concentration of  $48 \text{ mmol/m}^3$  in low latitudes is reached at 800 meters depth in year 2250, which is not shown in the figure. The maximum concentration in high latitudes is  $3.7 \text{ mmol/m}^3$  at 500 meters depth in year 2180.

Figure 19d represents the nitrate concentration profile in year 2200. In low latitudes the surface layer nitrate concentration is  $1.1 \text{ mmol/m}^3$ . The profile shows a steep increase to its maximum concentration of  $32.8 \text{ mmol/m}^3$  at 1300 meters depth. Furthermore, the concentration decreases to  $29 \text{ mmol/m}^3$  in the benthic area at 5500 meters depth. There is no substantial change in nitrate concentrations during the 500 year period, except in the top 200 meters in the high latitude ocean, where the concentration decreases from  $20.1 \text{ mmol/m}^3$  in 1750 to  $18.9 \text{ mmol/m}^3$  in 2250.

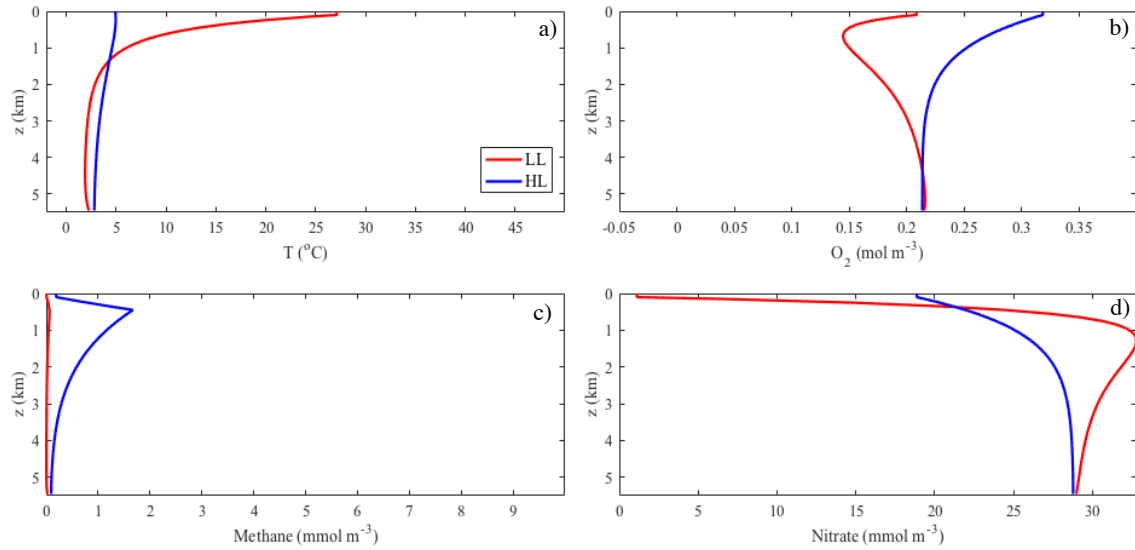


Figure 20: Depth profiles for scenario A2 with  $3^\circ\text{C}$  sensitivity for high- and low latitude ocean at simulation year 2150. (a) Temperature, (b)  $\text{O}_2$ , (c)  $\text{CH}_4$  concentration, (d) Nitrate concentration

Figure 20 illustrates four depth profiles regarding temperature variations,  $\text{O}_2$ -,  $\text{CH}_4$ - and nitrate concentrations for high- and low latitude ocean layers. The profiles present the A2 scenario with  $3^\circ\text{C}$  sensitivity at year 2150. The low latitude, temperature variations seen in Figure 20a, show a change in direction of the curve at 1000 meters depth where the inclination change from a horizontal direction to a vertical direction. This can be seen as a gradually decreasing curve from 0 meters to 1500 meters depth where the temperature decreases from  $27^\circ\text{C}$  to  $6^\circ\text{C}$ , before the temperature stabilizes between  $2^\circ\text{C}$  and  $3^\circ\text{C}$  between 1500 meter to 5500 meters depth. The high latitude temperature curve shows less variation from the surface and down to 5500 meters depth. The surface temperature is  $4.8^\circ\text{C}$ , where it gradually decreases down to  $2.7^\circ\text{C}$  at 5500 meters depth.

The structure of the  $\text{O}_2$  concentration profile is similar throughout the time period from year 1750 to 2250, but the concentrations vary. Figure 20b shows low latitude  $\text{O}_2$  concentrations that

are more rapidly decreasing in the upper ocean layers from  $0.21 \text{ mol/m}^3$  in the surface, to its minimum concentration of  $0.14 \text{ mol/m}^3$  at 700 meters depth. Thereafter, the concentration start to increase again, until it reaches  $0.22 \text{ mol/m}^3$  at 5500 meters depth. The high latitude concentration is gradually decreasing from the surface layer until 1500 meters depth, before the slope gets steeper from 1500 meters until 5500 meters depth. The  $\text{O}_2$  concentration start at  $0.32 \text{ mol/m}^3$  at the surface to  $0.21 \text{ mol/m}^3$  at the bottom depth.

An effect in the  $\text{CH}_4$  concentration can only be observed in high latitude layers, which indicates no  $\text{CH}_4$  release in low latitude. Figure 20c shows a maximum concentration of  $1.7 \text{ mmol/m}^3$  at 500 meters depth at year 2150. There is release of  $\text{CH}_4$  in the high latitude layer in year 2050 and 2130, which result in a continuous decreasing concentration from 500 meters depth until  $0 \text{ mmol/m}^3$  5550 meter.

The nitrate concentrations is stable at the different depths, throughout the time period from year 1750 to year 2250, with minimal variations. The surface nitrate concentration seen in Figure 20d is at its minimum value of  $1.1 \text{ mmol/m}^3$  in low latitude layers and  $18.9 \text{ mmol/m}^3$  in high latitude layers. The nitrate concentration increases with  $31.7 \text{ mmol/m}^3$  from the low latitude surface layer, until it reaches its maximum concentration of  $32.8 \text{ mmol/m}^3$  at 1300 meters depth. The concentration decreases thereafter, until it reaches  $29 \text{ mmol/m}^3$  at 5500 meters depth. The concentration interval is not as large for the high latitude ocean layers between the surface and the bottom layer. The nitrate concentration stabilizes at the maximum concentration of  $28.8 \text{ mmol/m}^3$  from 4600 meter to 5500 meters depth.

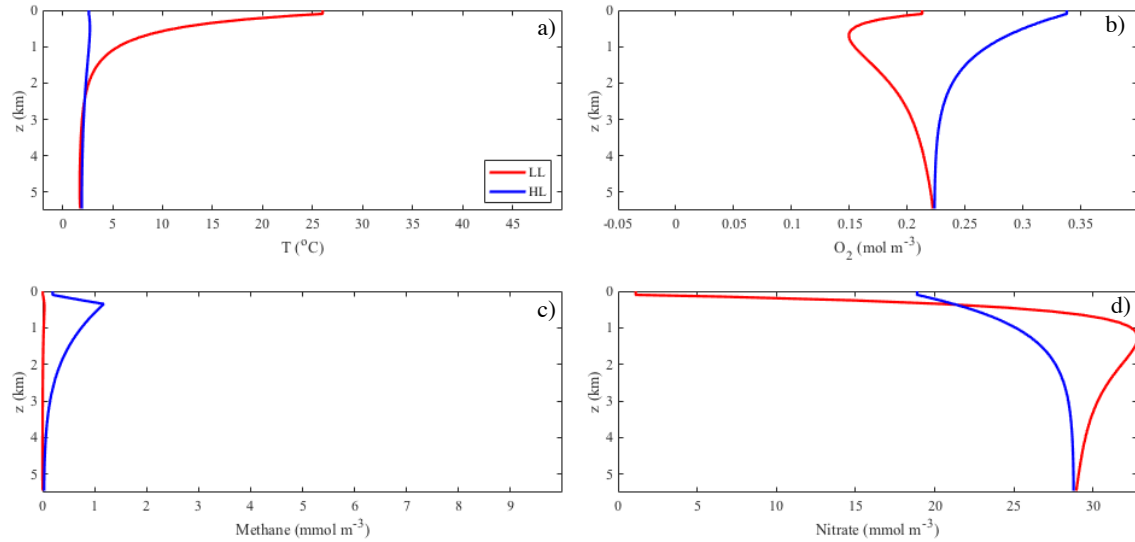


Figure 21: Depth profiles for scenario B1 with  $5^\circ\text{C}$  climate sensitivity for high latitude and low latitude ocean at simulation year 2050. (a) Temperature, (b)  $\text{O}_2$ , (c)  $\text{CH}_4$  concentration and (d) Nitrate concentration

Figure 21 shows profiles of scenario B1 with a  $5^\circ\text{C}$  climate sensitivity in 2050. In Figure 21a, the highest temperatures are observed in the surface layers, with  $26.8^\circ\text{C}$  in low latitudes and  $2.3^\circ\text{C}$  in high latitudes. For the entire 500 year simulation, the surface temperature reaches its maximum in 2130 with  $27^\circ\text{C}$  in low latitudes and in 2150 in high latitudes with  $3.8^\circ\text{C}$ . The low latitude ocean has a thermocline down to 2000 meters, thereafter the temperature stabilizes around  $2.5^\circ\text{C}$ . The



high latitude profile has a steady temperature range around 3°C.

In high latitudes, the  $O_2$  concentration decreases from 0.34 mol/m<sup>3</sup> in the surface layers to 0.22 mol/m<sup>3</sup> at 5500 meters depth, as illustrated in Figure 21b. The high latitude  $O_2$  concentration decreases from 0.22 mol/m<sup>3</sup> to 0.15 mol/m<sup>3</sup> in the first 800 m, thereafter it increases to its initial value of 0.22 mol/m<sup>3</sup> at 5500 meters depth.

Figure 21c, shows a  $CH_4$  concentration of 1.2 mmol/m<sup>3</sup> at 500 meters depth in 2050, a consequence of hydrate dissociation occurring in 2040. This is the maximum concentration observed, and the only release in the B1 (5°C) simulation with the given parameters in Section 5.3. By 2250, the  $CH_4$  of the whole ocean has been restored to its initial concentration of 0 mmol/m<sup>3</sup>. The low latitude  $CH_4$  remains around 0 mmol/m<sup>3</sup> throughout the timespan of the simulation.

Regarding the nitrate concentration profile in Figure 21d, the surface ocean concentration in high latitude is affected. Throughout the simulation period of 500 years, the concentration in the top 100 meters decreases steadily from 20.1 mmol/m<sup>3</sup> to 18.1 mmol/m<sup>3</sup>. The low latitude nitrate concentration remains unchanged from start to end. The low latitude concentration increases to 32.8 mmol/m<sup>3</sup> at 1200 meters depth and subsequently decreases to 29 mmol/m<sup>3</sup> at depth of 5500 meters.

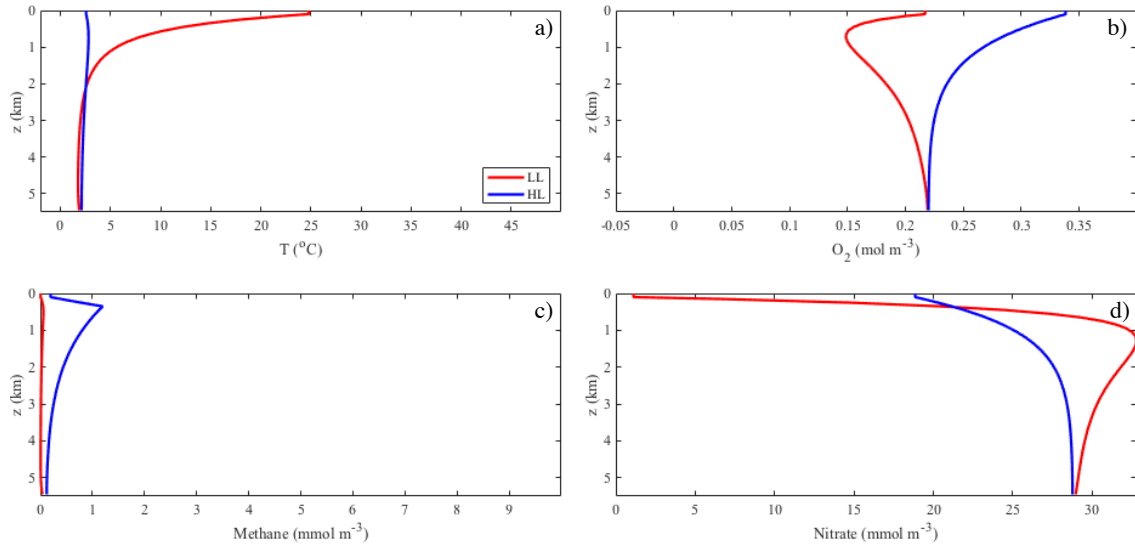


Figure 22: Depth profiles for scenario B1 with 3°C climate sensitivity for high latitude and low latitude ocean at simulation year 2070. (a) Temperature, (b)  $O_2$ , (c)  $CH_4$  concentration and (d) Nitrate concentration

Figure 22 presents the four depth profiles of temperature and  $O_2$ ,  $CH_4$ , and nitrate concentrations for the B1 scenario with 3°C sensitivity at year 2070. As seen in Figure 22a, the temperature is at its highest value, with 24.5°C at the surface in the low latitude layers. The temperature is thereafter decreasing until 1500 meters depth before the slope steepens. There is a relatively stable temperature of 2.5°C from 2000 meters depth to the bottom. The high latitude temperatures is 2.2°C at the surface, with show minimal variations throughout the depth profile. The maximum high latitude temperature is found to be 2.4 °C at 800 meters depth.

Figure 22b shows the  $O_2$  concentration profile in the ocean layers. The low latitude concentration is decreasing from  $0.21 \text{ mol/m}^3$  at the surface to its minimum concentration of  $0.15 \text{ mol/m}^3$  at 800 meters depth. From this depth the concentration start to increase again until it reaches its maximum concentration of  $0.22 \text{ mol/m}^3$  at 5500 meters depth. The  $O_2$  concentration at the surface is the maximum concentration in the high latitude layers with  $0.34 \text{ mol/m}^3$ . Thereafter the  $O_2$  concentration start decreasing and at 3000 meters depth it start stabilizing with minimal variations around its minimum concentration of  $0.22 \text{ mol/m}^3$ .

Figure 22c shows no  $CH_4$  release in the low latitude layers. A release is however observed in the high latitude layers, with maximum concentration of  $1.2 \text{ mmol/m}^3$  at 400 meters depth, as an effect of the hydrate dissociation at this depth in 2060. This is the only depth with a  $CH_4$  release in high latitude layers, which explains why the  $CH_4$  concentration decreases uniformly, until it reaches  $0 \text{ mmol/m}^3$  at 3600 meters depth.

The low latitude, nitrate concentration profile shows no variation throughout the 500 year time period simulated, while high latitude concentration at 100 meters depth, decreases from  $19.7 \text{ mmol/m}^3$  in 1750 to  $18.8 \text{ mmol/m}^3$  in 2250. The bottom layer at 5500 meters depth, show a minimal increase in the nitrate concentration of  $28.6 \text{ mmol/m}^3$  in 1750 to  $28.8 \text{ mmol/m}^3$  in 2250. The low latitude nitrate concentration at the surface is seen as the minimum concentration of  $1.1 \text{ mmol/m}^3$  in Figure 22d, before it rapidly increases to its maximum concentration of  $32.8 \text{ mmol/m}^3$  at 1300 meters depth. Thereafter, the nitrate concentration decreases to  $28.9 \text{ mmol/m}^3$  at 5500 meters depth.

### 6.3.2 Dissolved Inorganic Carbon and Alkalinity

In year 1750, the initial dissolved inorganic carbon (DIC) profile increased from  $2.0 \text{ mol/m}^3$  at the surface to  $2.3 \text{ mol/m}^3$  at 5500 meters depth, while the alkalinity (ALK) increases from  $2.40 \text{ eq/m}^3$  to  $2.44 \text{ eq/m}^3$  with depth. The plots in Figure 23 illustrates the relationship between alkalinity and dissolved inorganic carbon in high latitudes (blue) and low latitudes (red) by the end of the iteration process, year 2250.

In the A2(5°C) scenario (Figure 23a), which is the only scenario where low latitude  $CH_4$  release is observed, the end DIC has a maximum value of  $2.41 \text{ mol/m}^3$  at 900 meters depth. The alkalinity shows the inverse tendency, with its minimum value of  $2.40 \text{ eq/m}^3$  at the equivalent depth and time. At this extrema for both curves, DIC and ALK intersects. The end DIC in the surface is  $2.32 \text{ mol/m}^3$ , an increase by  $0.32 \text{ mol/m}^3$  from the 1750 value. In high latitudes, the alkalinity profile shows the same tendency with its maximum as the dissolved inorganic carbon is at its minimum. In the A2(3°C) scenario, seen in Figure 23b, is the end DIC concentration in the surface  $2.34 \text{ mol/m}^3$  in high latitudes and  $2.39 \text{ mol/m}^3$  in low latitudes. Also here, there is a inverse relationship between DIC and ALK, especially prominent at 800 meters depth and 5500 meters depth, where the DIC has its two maximum concentrations, both of  $2.4 \text{ mol/m}^3$ , and ALK has the inverse trend, with concentrations  $2.41 \text{ mol/m}^3$  and  $2.45 \text{ mol/m}^3$ , respective to increasing depth.

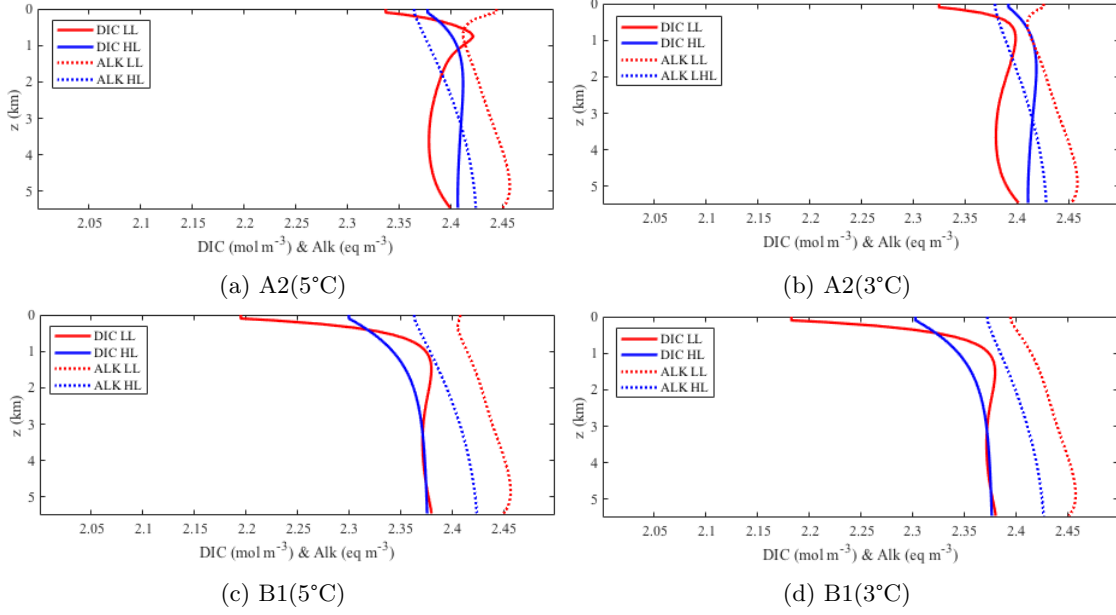


Figure 23: Dissolved inorganic carbon (DIC) and alkalinity (ALK) profile in year 2250.

Figure 23c and Figure 23d present the B1 scenarios with similar tendencies for both ALK and DIC throughout the depth profile. In low latitude layers the DIC concentration at the surface is  $2.19 \text{ mol/m}^3$  and  $2.18 \text{ mol/m}^3$  for respectively B1  $5^\circ\text{C}$  and  $3^\circ\text{C}$  sensitivity. DIC in low latitude layers increases with depth and reaches a maximum concentration of  $2.38 \text{ mol/m}^3$  at 1600 meters depth for both  $5^\circ\text{C}$  and  $3^\circ\text{C}$  sensitivity. It thereafter stabilize around the maximum value until it arrives at 5500 meters depth. The same tendency is seen in high latitude layers, where the DIC concentration at the surface is  $2.3 \text{ mol/m}^3$  for both sensitivities and increases with  $0.07 \text{ mol/m}^3$  before reaching 5500 meters depth. Alkalinity is stable throughout the depth profile, with minimal variation between the surface and 5500 meters depth in both high and low latitude layers. In low latitude layers alkalinity is ranging between  $2.40 \text{ mol/m}^3$  and  $2.45 \text{ mol/m}^3$ , while in high latitude layers it is ranging between  $2.36 \text{ mol/m}^3$  and  $2.43 \text{ mol/m}^3$ .

## 7 Discussion

### 7.1 Result Interpretation

In this section, the results of the simulation with the input parameters presented in Table 3 are interpreted. Methane hydrate stability and solubility have been calculated as functions of temperature, pressure and salinity conditions. Hydrates will destabilize and start releasing  $\text{CH}_4$  within the 500 year period between 1750 and 2250, independent of which combination of emission scenario and climate sensitivity is applied in the simulation.

The inventory size estimation was set to 63 Gt C in the upper continental slope. This is approximately 3 % of the total global inventory of 1800 Gt C. Only a fraction of the  $\text{CH}_4$  inventory in the upper continental slope is released prior to 2100, the apex year of the SRES scenarios developed by the IPCC. After the 500 year period, 0.6 %, 0.1 %, 0.06 % and 0.04 % of the total inventory of 1800 Gt C is released respectively for the A2(5°C), A2(3°C), B1(5°C) and B1(3°C) scenario. For perspective of the magnitude of the dissociating  $\text{CH}_4$ , the total anthropogenic  $\text{CH}_4$  flux is currently of  $2.3 \times 10^{13}$  mol C/year (IPCC, 2014). The total released  $\text{CH}_4$  in the simulation resides in the interval  $8.3 \times 10^{11}$  mol C/year and  $5.2 \times 10^{12}$  mol C over a timespan between 90 and 150 years, depending on scenario. Furthermore, just a fraction of the addressed total released  $\text{CH}_4$  is eventually released to the atmosphere. Thus, the emissions are of a significantly lower magnitude than the current anthropogenic  $\text{CH}_4$  flux to the atmosphere, and therefore most likely not a source of a natural disaster within the year 2250. The 95 % to 99 % of the global  $\text{CH}_4$  hydrate inventory, which is located in deep marine settings, is not a subject to destabilization, even under a prolonged simulation period of 1000 years. These deposits will endure for centuries to come because of prevailing temperature, salinity and pressure conditions, where the actual pressure does not become larger than the dissociation pressure and the hydrate solubility multiplied by layer area does not exceed the hydrate  $\text{CH}_4$  inventory of the layer.

The upper continental slope has a high susceptibility to intermediate to high level of warming of ocean water and the total hydrate inventory is subjected to evident change within 2250. Our model suggest that there is currently no hydrate present in more shallow depths than 400 meters. The hydrates destabilizing before 2100 are the most shallowly located hydrate deposits in the upper continental slope in areas of latitude greater than 52°, termed high latitude areas in this report and the DCESS model. In the Arctic area, this especially will affect the hydrates present in the north, north-east and north-west of Canada and north of Russia, referring to Figure 4. In the Antarctic, the deposits present in the south of South America are exposed. The observed high latitude hydrate dissociation is in accordance with simulation conclusions of Kvenvolden in 1988 and more recently Kretschmer et al. in 2015 (Kvenvolden, 1988) (Kretschmer et al., 2015). The methane hydrate stability zone depth transits to greater depths along the continental slope with time. The rate of which this shift depends on the climate conditions predicted. The more generous emission scenario selected by the user, the faster the rate of transition along the continental slope. The continuous warming of the world ocean will destabilize hydrates at depths down to 800 meters within 2250 in low latitudes in the A2(5°C) scenario. The remaining three scenarios experience dissociation down to 600 meters depth at slightly different times in the interval between the years 2060 and 2130 with the given input parameters. The methane hydrate stability zone will decrease in thickness with 300 meters in high latitudes and 100 meters in low latitudes under the A2(5°C) scenario. In the A2(3°C) scenario, the stability zone thickness decreases with 200 meters in high latitudes. In the remaining two scenarios, B1(5°C) and B1(3°C), the stability zone will decrease with 100 meters in high latitudes. All decrease starts at 400 meters in high latitudes and 800 meters in low latitudes. Warming of ocean water will destabilize hydrate deposits on the continental slope at depths down to 800 meters in low latitudes within 2250, if the A2(5°C) scenario matches the future.

Regarding the ocean, the release of  $\text{CH}_4$  has the ability to increase the ocean acidification and oxygen depletion. Aerobic  $\text{CH}_4$  oxidation consumes  $\text{O}_2$  and  $\text{CH}_4$  to generate  $\text{CO}_2$  and  $\text{H}_2\text{O}$ .  $\text{CO}_2$  has the ability to react with  $\text{H}_2\text{O}$  to create  $\text{H}^+$  and the highly acidic dissolved inorganic carbon species  $\text{HCO}_3^-$ . Furthermore, if oxidation by denitrification generates even more  $\text{CO}_2$ , the acidification is accelerated. None of the simulated scenarios with the chosen input parameters bypass aerobic oxidation. However, as the input parameters are highly uncertain, variation of these might lead to bypassing of aerobic oxidation and the start of the nitrogen dependent oxidation of  $\text{CH}_4$ . In this case, local anoxia and ocean acidification is plausible, where dissolved inorganic carbon exceeds the alkalinity. Alkalinity is the oceans ability to neutralize acid. Because oxygen in the ocean is not easily replenished, the consumption of oxygen might be critical for life forms at this depth, which are mostly dependent on oxygen. An increased  $\text{CO}_2$  concentration as a result of both climate change and  $\text{CH}_4$  oxidation is susceptible to dissolve and form  $\text{H}_2\text{CO}_3$ , leading to local ocean acidification as well as local oxygen depletion. The scenarios show no immediate sign of local anoxia or reduction in oceanic pH, based on the relation between alkalinity and dissolved inorganic carbon. However, with parameters of larger inventories of  $\text{CH}_4$  or more abrupt release, the rate of which oxygen and nitrate concentrations are depleted, and the sulphate dependent oxidation will take place. This reaction has the potential to intensify the acidification process.

Methane hydrate contribution to temperature and atmospheric greenhouse gas change is varying for the different scenarios with different sensitivities. Two causes can be attributed to hydrate dissociation induced increase in the atmospheric partial pressure of  $\text{CH}_4$ . First, a sufficient  $\text{CH}_4$  flux leads to  $\text{CH}_4$  bypassing  $\text{CH}_4$  reduction processes in the ocean. Secondly, limitations in the abundance of reducing agents, including oxygen, nitrate and sulphur concentrations, as well as the presence of  $\text{CH}_4$  reducing microorganisms might restrict  $\text{CH}_4$  removal in the ocean water, and thereby not efficiently remove all  $\text{CH}_4$  released. The A2 scenario with  $5^\circ\text{C}$  sensitivity, with a  $\text{CH}_4$  inventory of 63 Gt C in the upper continental shelves, gave a temperature rise of  $8.9^\circ\text{C}$  during the 500 year time period simulated. This results in a  $0.5^\circ\text{C}$  increase in temperature when comparing to a model simulation with zero methane hydrate contribution, indicating that methane hydrates alone were the cause of an additional  $0.5^\circ\text{C}$  rise in atmospheric temperature beyond the impact from the scenario. Furthermore, methane hydrate injection has impacted the atmospheric greenhouse gas concentrations, during the 500 year simulation. The  $\text{CH}_4$  concentration rises with 72.4 % if zero  $\text{CH}_4$  is injected into the atmosphere, while a methane hydrate contribution will cause the  $\text{CH}_4$  concentration to rise with 180 % of the pre-industrial value. This implies that the atmosphere in 2250 will have double the  $\text{CH}_4$  concentration, than predicted only by the A2 scenario with  $5^\circ\text{C}$  sensitivity. The methane hydrates will affect the  $\text{CO}_2$  concentration in the atmosphere in a smaller scale, with 1.03 times higher  $\text{CO}_2$  concentration in the atmosphere compared with zero methane hydrate contribution.

The A2 scenario with  $3^\circ\text{C}$  sensitivity gives a  $5.2^\circ\text{C}$  increase in atmospheric temperature during the 500 year estimation. The temperature increase is  $0.1^\circ\text{C}$  higher in 2250 with a methane hydrate release compared to without. The greenhouse gas concentrations is also affected, where the  $\text{CH}_4$  concentration has increased with 82.3 % over 500 years, compared to 63.8 % increase with zero methane hydrate release.  $\text{CH}_4$  released in the B1 scenario with  $5^\circ\text{C}$  sensitivity constitute 9.2 % of the amount released in the A2 scenario with  $5^\circ\text{C}$  sensitivity. The B1 scenarios show minimal impact from methane hydrate dissociation in both temperature and atmospheric gases, as only one layer in high latitude contributes to a  $\text{CH}_4$  injection to the ocean. This impact is too small to have an effect on the atmospheric gas concentrations and temperature. Forcings in the A2 scenario with  $5^\circ\text{C}$  sensitivity, contribute to a high temperature increase in the atmosphere, affecting methane hydrate dissociation in both low and high latitude ocean layers. This scenario therefore

has the most abundant  $\text{CH}_4$  release from hydrate, with a prominent impact on temperature and atmospheric gas concentrations, compared to the other scenarios. The detailed calculations of the scenarios in comparison to zero methane hydrate model simulation, can be found in Appendix III.

## 7.2 Sensitivity Analysis

The simulations performed in the sensitivity analysis are all based on the A2 scenario with a  $5^\circ\text{C}$  climate sensitivity, as the most extreme scenario is expected to produce the most perceptible results. The sensitivity analysis is subdivided in two segments, the first being model sensitivity to inventory size. In the second segment, the model sensitivity with regards to the total release time after the conditions of dissociation have been fulfilled, is analyzed.

### 7.2.1 Methane Hydrate Inventory

Figure 24 shows a linear relation between the  $\text{CH}_4$  inventory and  $\text{CH}_4$  release in both high latitudes and low latitudes. All simulations have been run with the A2( $5^\circ\text{C}$ ) scenario and total release time after dissociation of 90 years. Furthermore, oceans of depth 400 meters to 1400 meters in high latitudes and 800 meters to 1400 meters in low latitudes have an uniformly distributed  $\text{CH}_4$  inventory. Both linear regressions have a coefficient of determination ( $R^2$ ) of 0.99, indicating virtually no variation. The low latitude Gt C relation has a more steep increase, as the inventory in each ocean layer is 84% of the total, while the high latitude inventory consists of the remaining 16%, and therefore has a less steep increase in release as a function of inventory size.

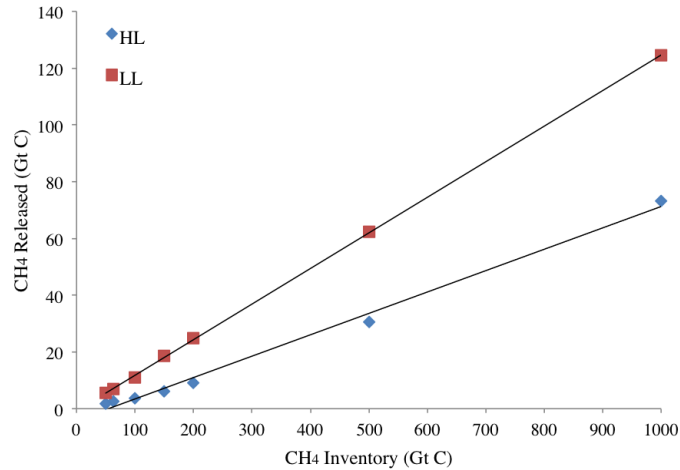


Figure 24: The linear relation between  $\text{CH}_4$  inventory size and magnitude of  $\text{CH}_4$  released from hydrates in the A2( $5^\circ\text{C}$ ) scenario.

Figure 25a and Figure 25b illustrate  $\text{CO}_2$  and  $\text{CH}_4$  variations in the atmosphere with  $\text{CH}_4$  hydrate inventories of 100 Gt C, 200 Gt C and 500 Gt C located in the upper continental shelves. Both partial pressures show an increase with increasing inventory size. The  $\text{CH}_4$  partial pressure is directly linked to the amounts of  $\text{CH}_4$  surpassing reduction processes in the ocean sediment and water column. A wide spread response forking after initial release in 2040 is observed. The atmospheric lifetime of  $\text{CH}_4$  increases with the abundance of the gas, as the hydroxyl radical abundance in the atmosphere is reduced when it reacts with  $\text{CH}_4$ . In the event of a surplus  $\text{CH}_4$  after the OH radical inventory is reduced significantly, the reduction rate of  $\text{CH}_4$  in the atmosphere

ceases, and  $\text{CH}_4$  starts accumulating. Figure 25b illustrates this phenomenon. With an inventory of 100 Gt C, pulses of  $\text{CH}_4$  to the atmosphere are effectively reduced, while with an inventory of 500 Gt C, the atmosphere is saturated with  $\text{CH}_4$  and OH radicals are no longer present at a sufficient concentration to reduce the abundance of  $\text{CH}_4$ . Consequently, the atmospheric lifetime of  $\text{CH}_4$  increases. The  $\text{CO}_2$  partial pressure increases as a response to reactions between OH-radicals in the atmosphere and the emitted  $\text{CH}_4$ . Furthermore, ocean temperature increase reduces  $\text{CO}_2$  solubility, whereas more  $\text{CO}_2$  is vectored to the atmosphere by bubble stripping.

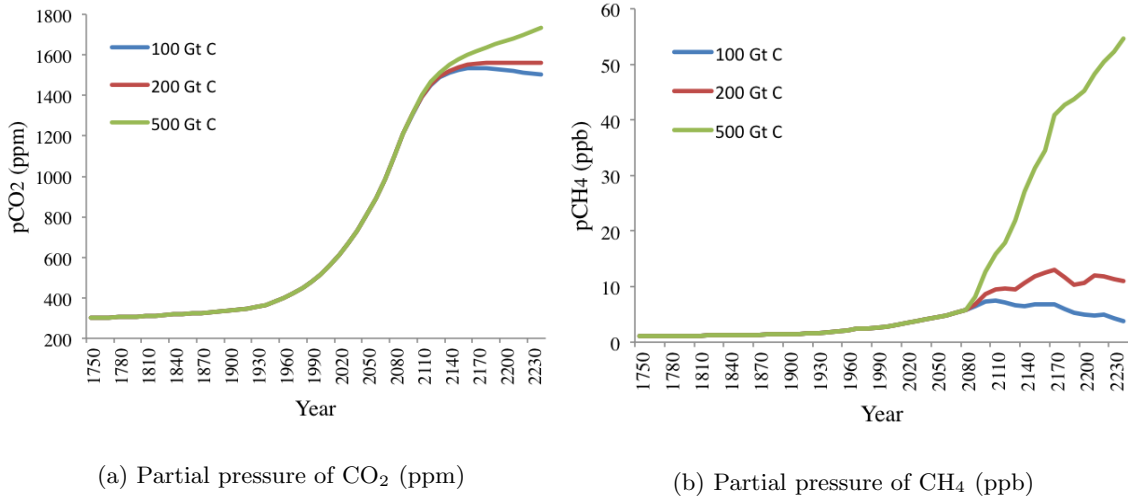


Figure 25: Atmosphere results for 500 year simulations for 100 Gt C (blue), 200 Gt C (red) and 500 Gt C (green)  $\text{CH}_4$  inventory

$\text{CH}_4$  directly injected to the ocean from hydrates has effects on the oceanic conditions. Increasing  $\text{CH}_4$  oxidation leads to denitrification, which leads to additional  $\text{CO}_2$  release to the ocean and eventually atmosphere. With an input  $\text{CH}_4$  inventory in hydrates of 150 Gt C and a 1000 year simulation, low latitude depths of 800 meters start dissociating in 2180. Up to this point, the oxygen content at this depth has steadily been of  $0.14 \text{ mol/m}^3$ . When  $\text{CH}_4$  is released, oxidation of  $\text{CH}_4$  starts. Within the following 40 years, the oxygen in depths between 600 and 1000 meters is depleted to less than  $3 \text{ mmol/m}^3$  ( $\text{O}_{2\min}$ ). Under suboxic/anoxic conditions, nitrate-dependent microbial anoxic  $\text{CH}_4$  oxidation takes place. A steady initial concentration of  $32 \text{ mmol}$  nitrate per  $\text{m}^3$  is decreased to  $1 \text{ mmol/m}^3$  in the 100 year period between 2180 and 2280, being lower than the minimum nitrate concentration of  $0.03 \text{ mmol/m}^3$  ( $\text{NO}_{3\min}$ ). Furthermore, denitrification produces  $\text{CO}_2$ , impacting  $\text{pCO}_2$  to increase. The  $\text{CO}_3$  concentration also decreases in the same period, indicating that the sulphate dependent microbial AMO occurs, and that the increased  $\text{pCO}_2$  leads to more acidic ocean conditions, which drives calcite dissolution. The sulphate dependent reaction occurs when both oxygen and nitrate is depleted. In conclusion, an inventory size equal to or larger than 150 Gt C in scenario A2(5°C) with 90 years release time after destabilization, will result in surpassing of aerobic  $\text{CH}_4$  oxidation, and lead to cascading AMO reactions consuming nitrate and sulphate. Local anoxia and ocean acidification is plausible as the inventory size still is a subject of research.

In Appendix IV, the calculation of the linear regression of the  $\text{CH}_4$  inventory and  $\text{CH}_4$  release is included, as well as the sensitivity analysis with regards to  $\text{pCO}_2$ ,  $\text{pCH}_4$  and atmospheric temperature.

### 7.2.2 Release Time

The release time for hydrate dissociation is calculated using the maximum and minimum contemporary global  $\text{CH}_4$  fluxes of 16 and 3200 Tg  $\text{CH}_4$  per year, as input in Equation 21 found in Appendix IV (Ruppel and Kessler, 2016). Together with a methane hydrate inventory of 63 Gt C, the release time interval is calculated to lay between 0.5 years and 90 years for high latitude layers and between 0.5 years and 140 years for low latitude layers. The maximum release time calculated at 90 years for high latitude layers, has been used in the model simulations presented in results. As this is one of the extremity values it is reason to believe that a model simulation with lower dissociation release time, will result in different  $\text{CH}_4$  release outcomes. The output data further discussed in this section, can be found in Appendix IV.

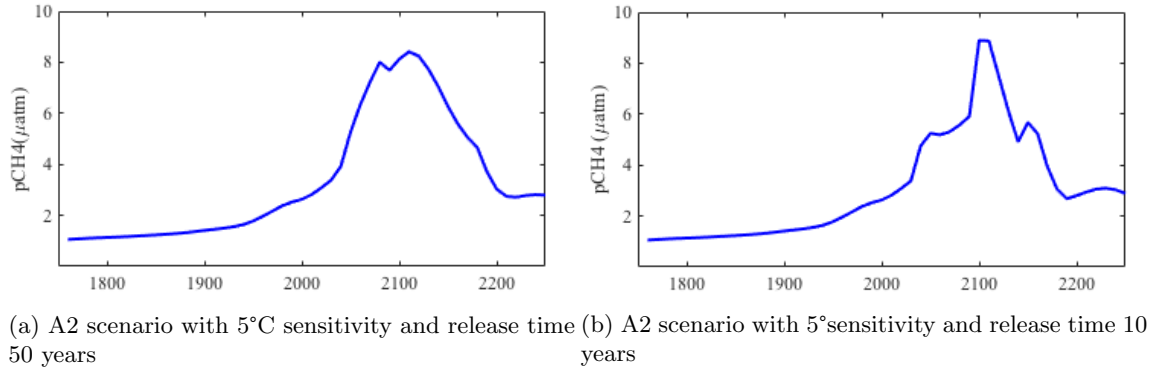


Figure 26: Sensitivity of release time from methane hydrate

Figure 26 presents two model simulations with alternative release times, within the calculated release time interval, at 10 and 50 years. Model simulation with a release time of 90 years resulted in a maximum  $\text{CH}_4$  concentration of 8.6  $\mu\text{atm}$ , as observed in Figure 15b. Lowering the release time to 10 and 50 years resulted in various maximum  $\text{CH}_4$  concentrations observed in the atmosphere. Figure 26a presents a  $\text{CH}_4$  release of 8.4  $\mu\text{atm}$  in 2120, while Figure 26b presents a  $\text{CH}_4$  release of 8.9  $\mu\text{atm}$  in 2100. Figure 26a and 26b would expectantly present higher maximum concentrations compared to Figure 15b, as the simulations contain the same amount of  $\text{CH}_4$  inventory, which would create a more concentrated release. Figure 26a deviates from this estimation as it obtains a lower maximum concentration than Figure 15b. The lower release time has affected the time period where  $\text{CH}_4$  is released from the ocean layers, but not the year at which the ocean layer start releasing. When release time is 50 years the first ocean layers in high latitude start releasing  $\text{CH}_4$  in year 2040, which means the layer will be empty in year 2090. As the next ocean layer in high latitude does not start releasing  $\text{CH}_4$  until year 2100, this indicates a time period of 10 years where no  $\text{CH}_4$  is injected from ocean layers, and atmosphere sinks start removing  $\text{CH}_4$ . This is observable as a small decline in the  $\text{CH}_4$  curve after year 2090. Figure 26b shows abrupt variations in the  $\text{CH}_4$  curve as large  $\text{CH}_4$  concentrations is released over a short period of time, together with the scenario initiation from year 2000. Figure 26b shows the same tendencies as Figure 26a, but with steeper declines in the  $\text{CH}_4$  curve, indicating the time interval where no  $\text{CH}_4$  is injected and the atmospheric sinks start removing  $\text{CH}_4$ . The scenario maximum duration in 2100 will amplify the  $\text{CH}_4$  release in 2100, achieving the maximum  $\text{CH}_4$  concentration in the atmosphere. A release time of 50 years entails a more continuous supply of  $\text{CH}_4$  injection into the atmosphere, compared to a 10 year release time. This affects the residence time of  $\text{CH}_4$  in the atmosphere as well as the atmospheric sinks. This is observed in Figure 26a, where the  $\text{CH}_4$  concentration is decreasing more gradually after maximum concentration has been released, compared to Figure 26b.



### 7.3 Comparison to Historic Hydrate Dissociation

Historically, there are indications that methane hydrate dissociation has been the reason for past hyperthermal events. PETM is of particular interest as it is one of the most widely studied, past hyperthermal events, and can provide an analog for future climate and environmental change if anthropogenic CO<sub>2</sub> emissions continue on their current path. An important difference between PETM and the current age, is that mean climate already had been quite warm during tens of millions of years during Paleocene in the PETM. Within 10000 to 30000 years, the temperature increased with 4°C to 5°C in low latitudes and 6°C to 8°C in high latitudes. The model simulation for A2 and B1 scenarios, showed temperature increase between 2.7°C and 8.9°C in low latitudes and between 2.0°C and 7.6°C increase in high latitudes during contemporary climate change. This simulation predicted the temperature change during 500 year from pre-industrial time. Compared to the PETM temperature rise, this is a more abrupt increase in temperature than ever measured before.

Studies have found the carbon release rate to the ocean-atmospheric system during PETM to  $< 1.1 \text{ Pg/yr}^{-1}$ , which is comparable to the present release rate at 0.016 to 3.2  $\text{Pg/yr}^{-1}$  (Ruppel and Kessler, 2016). The release time the hydrate are dissociating and injecting CH<sub>4</sub> from the ocean, were calculated to 90 years, using the lowest release rate of 0.016  $\text{Pg/yr}^{-1}$ . The estimated release rate is used as a simplification throughout the simulation, even though it preferably should increase as the CH<sub>4</sub> release increased. This indicates that higher CH<sub>4</sub> emissions from the ocean seafloor in the future would affect the contemporary release rate to increase to even higher rates than seen during PETM. A rapid release of large volume of CH<sub>4</sub> will have the potential to inject more CH<sub>4</sub> into the atmosphere as the CH<sub>4</sub> might bypass strong sediment or water column sinks (Ruppel and Kessler, 2016).

The model simulation is based on a total CH<sub>4</sub> inventory of 1800 Gt C, where 63 Gt C exist in the upper continental slope, which is where dissociation is estimated to occur. This estimation constitute a small fraction of the methane hydrate injection of 1100 Gt C to 2100 Gt C during PETM. However, calculations based on instantaneous release of 1.8 Gt C from the methane hydrate reservoir (0.1% of total CH<sub>4</sub> inventory) reveal a temporary increase in atmospheric CH<sub>4</sub> concentrations by more than 60 % if all of the gas reaches the atmosphere (Ruppel and Kessler, 2016). This gives an indication of the potential effect methane hydrate dissociation can have on contemporary climate even by small CH<sub>4</sub> contributions, relative to the PETM.

### 7.4 Limitations and Uncertainties

The stabilization effect from sea level rise has not been accounted for and will conceivably counteract some of the destabilization predicted in the model. However, sea level projections by the IPCC predict a rise of less than 2 metres by 2100, not enough to impact stability of hydrates significantly, because hydrates are more sensitive to temperature than pressure conditions (Beaudoin et al., 2014a). Furthermore, the hydrate implementation covers the hydrates present in marine environment. Emphasis has been put on the upper continental shelves, which prove to have a high susceptibility to climate change. The deep marine inventory has a low susceptibility to climate change. Three main hydrate domains are left; the onshore permafrost, subsea permafrost and subglacial. Especially the latter has a high susceptibility to climate change due to thawing of ice sheets, and should be included in the future ice module of the DCESS model. The permafrost settings are expected to have an intermediate susceptibility to climate change. There is a natural

conflict when modelling on a global scale, as regional refinement with local parameterization might produce a more plausible output. The results in this report state that hydrates located in high latitude oceans are more sensitive to climate change, which is interesting to investigate on a local scale.

An overall challenge is utilizing suitable assumptions when running the model. Reliable data regarding inventory, distribution, both geographically and geologically, biogeochemical sink processes and climate forcing scenarios are crucial for a representative, quantitative result. The first challenge with obtaining realistic results from the simulation is utilizing a reliable  $\text{CH}_4$  hydrate inventory size. Figure 27 illustrates global hydrate size estimations from other reports, which range between 300 and 3000 Gt C. In this reports calculations, an inventory of 1800 Gt C has been chosen (Ruppel and Kessler, 2016). The general tendency, as depicted in Figure 27, is that the size estimations have been decreasing since the 1980s.

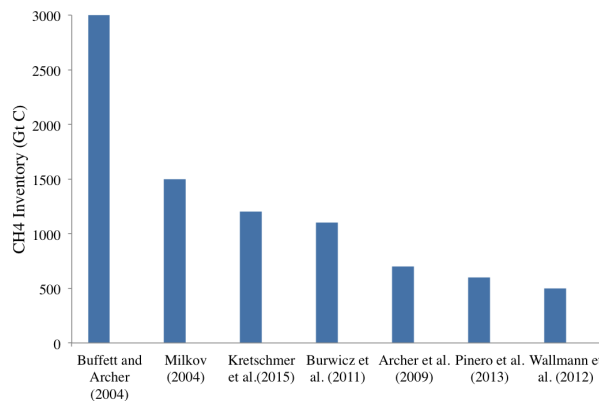


Figure 27: Global  $\text{CH}_4$  inventories in selected previous estimations (Kretschmer et al., 2015)

The  $\text{CH}_4$  hydrate module calculates release of  $\text{CH}_4$  to the ocean sediment based on thermodynamic, empirical equations regarding hydrate stability and solubility as a function of temperature, salinity and pressure, developed by Tishchenko et al. in 2005 (Tishchenko et al., 2005). It does not include the rate of thermogenic and methanogenic  $\text{CH}_4$  generation in situ or below the methane hydrate stability zone which potentially supplies methane hydrate generation and regeneration. Even further, the abundance of methane hydrates is dependent on the local lithology and sediment properties in terms of e.g. porosity and permeability. The current model does include a sediment subfunction in the hydrate module, and the inventory and dissociated magnitude is therefore a subject of overestimation.

The next model validity confrontation features the complexity of the  $\text{CH}_4$  sinks incorporated. As stated by Ruppel et al, the nature of  $\text{CH}_4$  sinks in the sediment setting, water column and atmosphere is still a subject of research, and not completely understood in respect to strength and quantity (Ruppel and Kessler, 2016). In the sediment, gas bubbles might be trapped as a result of the lithological conditions and prevented from interaction with the water column. In general, the sediments function as a sink of  $\text{CH}_4$  is not understood in detail, as the hydrate-related sediment module is missing. In addition to the already incorporated AOM sink, a non-AOM geochemical sink will likely increase the result validity. Furthermore, limitations to  $\text{CH}_4$  oxidation from e.g. nutrient supply might take place in certain settings. The fate of  $\text{CH}_4$  in the ocean-atmosphere boundary layer is also an important factor in quantifying the  $\text{CH}_4$  released to the atmosphere. In the DCESS model, the simplified sink processes included, are  $\text{CH}_4$  oxidation for oxic conditions,

nitrate-dependent microbial AMO for suboxic conditions and sulphate dependent microbial AMO for anoxic conditions in the ocean, together with atmospheric oxidation.

Another improvement of the model would be to account for the variations in ocean circulation system due to climate change, and how they affect the  $\text{CH}_4$  migration pathway. Variations in direction and temperature distribution might impact the methane hydrate dissociation trends in segments of the ocean. An implementation of the relation between ocean currents and a sea-ice and glacial module in the DCESS model is a natural next step to simulate variations in ocean currents and temperatures. Incorporation of permafrost based methane hydrate in such a module is possible, and thereby gives a more complete understanding of the global methane hydrate inventories' response to climate change.

## 8 Conclusion

The atmospheric greenhouse gas concentrations and temperature were largely influenced by methane release from hydrates during simulation of A2 scenario with 5°C sensitivity, compared to the other scenarios. The 500 year simulation showed a temperature increase 0.5°C higher in 2250, than the temperature simulated with zero methane hydrate contribution. Furthermore, the CH<sub>4</sub> concentration in the atmosphere rose to 180 % of the pre-industrial value, almost double the CH<sub>4</sub> concentration when no methane is injected from hydrates. The atmospheric CO<sub>2</sub> concentration was 1.03 times higher in 2250 in contrast with zero methane release from hydrates. Methane hydrate dissociation resulted in a minimal atmospheric variations for the other scenarios, compared to no methane hydrate contribution, indicating that a substantial CH<sub>4</sub> release is needed to be able to amplify the scenarios. Despite a large CH<sub>4</sub> release in the A2 scenario with 5°C sensitivity compared to the other scenarios, is the release still negligible on a global scale, compared to the current anthropogenic releases of methane and other greenhouse gases, predicted in the scenarios.

Multiple aspects of the environment can be affected as a consequence of methane release. In addition to climatic impact in the atmosphere, methane oxidation within the ocean can contribute to acidification. This can affect the amount of dissolved oxygen, carbon dioxide, and other compounds in the ocean, in the way of denitrification and sulphate reduction, but none of the simulated scenarios with chosen input parameters bypass aerobic conditions.

The results presented in this thesis indicates that the warming rates predicted in the scenarios have a low impact on methane hydrate dissociation to the ocean-atmospheric system over the next century. Approximately 3 % of the world's methane hydrates exist in the upper continental slope, where the hydrates are at risk of being destabilized. This diminishes the potential of methane affecting the greenhouse gas concentrations, as it is rather consumed in the sediment or water column before entering the atmosphere. The scenario initiates in early 2000 and its impact on the methane hydrate dissociation is first observed in 2040. The contemporary anthropogenic climate change has not yet appeared to have triggered a significant amount of methane hydrate dissociation to this day.

Improvement of the understanding of methane hydrate and contemporary climate changes impact on its destabilization, require a more detailed estimate of hydrate inventories and release rate. Present day total global methane hydrate inventories vary between 300 and 3000 Gt C, which leads to high uncertainties when predicting the potential of methane release. Additionally, implementation of a methane hydrate sediment segment is needed to better quantify the amount of dissociated CH<sub>4</sub> released from the sediment and into the atmosphere. Uncertainties regarding the amount of CH<sub>4</sub> removed within the water column due to microbial sinks, are too large to create reliable estimates on the impact of destabilized methane hydrate into the environment.

## References

- Archer, D. (2007). Methane hydrate stability and anthropogenic climate change. *Biogeosciences*, 4(2):993–1057.
- Beaudoin, Y., Dallimore, S., Boswell, R., and Waite, W. (2014a). Frozen Heat: A UNEP Global Outlook on Methane Gas Hydrates, Executive Summary. Technical report, United Nations Environment Programme.
- Beaudoin, Y. C., Waite, W., Boswell, R., and Dallimore, S. R. (2014b). *Frozen Heat: A UNEP Global Outlook on Methane Gas Hydrates*, volume 1. GRID Arendal.
- Beaudoin, Y.C., Dallimore, S.R., Boswell, R. (2014). *Frozen Heat: A UNEP Global Outlook on Methane Gas Hydrates*, volume 2. GRID Arendal.
- Buffett, B. A. (2000). *Clathrate Hydrates*. Department of Earth and Ocean Sciences, University of British Columbia, Vancouver.
- Crespo-Medina, M., Twing, K. I., Kubo, M. D. Y., Hoehler, T. M., Cardace, D., McCollom, T., and Schrenk, M. O. (2014). Insights into environmental controls on microbial communities in a continental serpentinite aquifer using a microcosm-based approach. *Frontiers in Microbiology*, 5(NOV):1–9.
- Demirbas, A. (2010). *Green Energy and Technology: Methane Gas Hydrate*. Springer London, Trabzon, Turkey.
- Englezos, P. (1993). Clathrate Hydrates. Technical Report 7, Department of Chemical Engineering, The University of British Columbia, Vancouver.
- Heriot Watt University (2016). Institute of Petroleum Engineering - Heriot-Watt University: Centre for Gas Hydrate Research: Why are Gas Hydrates Important?
- Higgins, J. A. and Schrag, D. P. (2006). Beyond methane: Towards a theory for the Paleocene-Eocene Thermal Maximum. *Earth and Planetary Science Letters*, 245(3-4):523–537.
- IPCC (2000). IPCC Special Report: Emission Scenarios: Summary for Policymakers. Technical report, Intergovernmental Panel on Climate Change.
- IPCC (2014). Climate Change 2014 Synthesis Report Summary Chapter for Policymakers. *Ipcc*, page 31.
- Khokhar, A., Gudmundsson, J., and Sloan, E. (1998). Gas storage in structure H hydrates. Technical report, Norwegian University of Science and Technology, Department of Petroleum Engineering and Applied Geophysics, Trondheim.
- Kretschmer, K., Biastoch, A., Rupke, L., and Burwicz, E. (2015). Modelling the fate of methane hydrates under global warming. *Global Biogeochemical Cycles*, 29:610–625.
- Kvenvolden, K. A. (1988). Methane Hydrates and Global Climate. *Global Biogeochemical Cycles*, 2(3):221–229.
- Liu, J., Liu, H., Xu, J., Chen, G., Zhang, J., and Wang, S. (2015). Chemical Physics Letters Structure and stability of multiply occupied methane clathrate hydrates. Technical report, School of Chemistry and Chemical Engineering, Jinan, China.
- Lonero, A. (2008). How are Methane Hydrates Formed, Preserved, and Released?

- Pierrehumbert, R., Abbot, D., Voigt, a., and Koll, D. (2011). Climate of the Neoproterozoic. *Annual Review of Earth and Planetary Sciences*, 39(1):417–460.
- R. Dickens, G., R. O’Neil, J., K. Rea, D., and M.Owen, R. (1995). Dissociation of oceanic methane hydrate as a cause of the carbon isotope excursions at the end of Paleocene. *Paleoceanography*, 10(6).
- Ruppel, C. and Kessler, J. D. (2016). The Interaction of Climate Change and Methane Hydrates. *Reviews of Geophysics*, pages 1–43.
- Shaffer, G., Olsen, S. M., and Pepke Pedersen, J. O. (2008). Presentation, calibration and validation of the low-order, DCESS Earth System Model (Version 1). *Geosci. Model Dev.*, pages 17–51.
- Tishchenko, P., Hensen, C., Wallmann, K., and Wong, C. S. (2005). Calculation of the stability and solubility of methane hydrate in seawater. *Chemical Geology*, 219(1-4):37–52.

## Appendices

### Appendix I: Matlab Code - Methane Hydrate Implementation (AtmMet\_M.m)

Necessary changes have been made to the matlab code in both ODE\_M and THILDA\_M.m to incorporate AtmMet\_M.m in the DCESS model.

```
1 function [mpr,mdr] = AtmMet_M(t,MHM,AT,LL,HL)
2
3 % Input : t - time
4 %         At - atmospheric tracers
5 % Output: mpr(1) - MH release to atmosphere, 12C. mol/sec
6 %         mpr(2) - MH release to atmosphere, 13C. mol/sec
7 %         mpr(3) - MH release to one ocean layer, 12C. mol/sec LL
8 %         mpr(4) - MH release to one ocean layer, 13C. mol/sec LL
9 %         mpr(5) - MH release to one ocean layer, 12C. mol/sec HL
10 %        mpr(6) - MH release to one ocean layer, 13C. mol/sec HL
11 %        mdr(1) - methane oxydation in the atmosphere, 12C, mol/sec
12 %        mdr(2) - methane oxydation in the atmosphere, 13C, mol/sec
13
14
15 global sy rVa mgt R13pdb mdts2 methc13 dm d n c relLL trelLL tstopLL
    dtout tfrelLL trelHL tstopHL relHL tfrelHL aLL GAw dv GAc tend
    reltimeLL reltimeHL
16
17
18 %ATMOSPHERIC METHANE
19 %-----
20 pCH4o = 0.72e-6; %Pre-industrial methane
    concentration in atmosphere
21 pCH4 = AT(2,1); %Methane concentration in
    atmosphere
22 fatm=1.0039; %Fractionation in
    atmospheric oxidation
23 M = (pCH4-pCH4o)/pCH4o;
24
25
26 RCH4o = 1/(rVa*mdts2*sy); %PA decay rate for methane
    , residence time 8.4 yrs
27 RCH4 = RCH4o*(1-0.78*M/(M+11));
28
29 if (t/sy>=MHM(1))
30     mpr(1) = (mgt*MHM(2)*(t/sy-MHM(1))^4*exp(-MHM(3)*(t/sy-MHM(1))))/sy
    ;
31     mpr(2) = (mgt*MHM(2)*(t/sy-MHM(1))^4*exp(-MHM(3)*(t/sy-MHM(1))))/sy
    *(methc13*1e-3+1)*R13pdb;
32 else
33     mpr(1)=0;
34     mpr(2)=0;
35 end
```

```

36
37 mdr(1) = pCH4*RCH4; % atmospheric methane
      oxidation to CO2
38 mdr(2) = (pCH4*RCH4*AT(7,1)/pCH4)*fatm;
39
40
41 %OCEANIC METHANE
42 %-----
43 MHTot= 1800*mgt; %mol C % methane hydrate inventory
44
45
46
47 % Low Latitude MH Dissociation
48 %-----
49 TLL=LL(1,:) + 273.15; % Ocean temperature LL (
      Kelvin)
50 SLL=LL(2,:); % Ocean salinity LL
51
52
53 for nlayLL=8:14
54     P=(1+([dm/2 dm+(1:n-1)*d-d/2])/10)/10; % Pressure [MPa]
55     PdisLL(nlayLL)=(exp(-1.6444866*10.^3-0.1374178*TLL(nlayLL)
      +(5.4979866*10.^4/TLL(nlayLL))+2.64118188*10.^2*log(TLL(nlayLL)
      )+SLL(nlayLL)*(1.1178266*10.^4+7.67420344*TLL(nlayLL)
      -4.515213*10.^-3*TLL(nlayLL).^2-(2.04872879*10.^5/TLL(nlayLL))
      -2.17246046*10.^3*log(TLL(nlayLL)))+SLL(nlayLL)
      .^2*(1.70484431*10.^2+0.118594073*TLL(nlayLL)-7.0581304*10.^-5*
      TLL(nlayLL).^2-(3.09796169*10.^3/TLL(nlayLL))-33.2031996*log(
      TLL(nlayLL))))); %Hydrate dissociation pressure [MPa]
56     lnSolEq(nlayLL)=-2.5640213*10.^5-1.6448053*10.^2*TLL(nlayLL)
      +9.1089042*10.^-2*TLL(nlayLL).^2+4.90352929*10.^6/TLL(nlayLL)
      +4.93009113*10.^4*log(TLL(nlayLL))+SLL(nlayLL)
      *(-5.16285134*10.^2-0.33622376*TLL(nlayLL)+1.88199047*10.^-4*TLL(
      nlayLL).^2+9.76525718*10.^3/TLL(nlayLL)+9.9523354*10.^1*log(TLL(
      nlayLL)));
57     Sol(nlayLL)=exp(lnSolEq(nlayLL)+(5.04597*10.^-2+7.64415*10.^-4*SLL(
      nlayLL)-(3.90236*10.^-4+5.48947*10.^-6*SLL(nlayLL))*TLL(nlayLL)
      +(7.06154*10.^-7+9.87742*10.^-9*SLL(nlayLL))*TLL(nlayLL).^2)*(P
      (nlayLL)-PdisLL(nlayLL)))+(7.57285*10.^-5-1.90867*10.^-8*SLL(
      nlayLL)-1.4483*10.^-10*SLL(nlayLL)
      .^2-(1.96207*10.^-7-6.67456*10.^-11*SLL(nlayLL))*TLL(nlayLL))*
      (P(nlayLL)-PdisLL(nlayLL)).^2); %Hydrate solubility [mol C/kg]
58     VwLL=aLL.*GAw.*dv; % Volume of water in ocean
      layers [m3]
59     Dw=1028; % Water density [kg/m3]
60
61
62     if P(nlayLL) < PdisLL(nlayLL)
63

```



```

64     if Sol(nlayLL)*VwLL(nlayLL)*Dw>(MHtot*0.84)/(14-8) && trelLL(
        nlayLL)==0
65         trelLL(nlayLL)=t;
66         tstopLL(nlayLL)=trelLL(nlayLL)+reltimeLL(nlayLL);
67
68
69         if trelLL(nlayLL)<=dtout*sy
70             reltimeLL(nlayLL)=tend*sy;
71             tstopLL(nlayLL)=trelLL(nlayLL)+tend*sy;
72         end
73     end
74
75     if dtout*sy>reltimeLL(nlayLL) && trelLL(nlayLL)>0 && t<tstopLL(
        nlayLL)
76         relLL(nlayLL,c)=(MHtot*0.84)/(14-8);
77     end
78
79     if trelLL(nlayLL)>0 && tstopLL(nlayLL)>dtout*sy && t<tstopLL(
        nlayLL) && sum(relLL(nlayLL,:),2) < (MHtot*0.84)/(14-8)
80         relLL(nlayLL,c)=(((MHtot*0.84)/(14-8))/reltimeLL(nlayLL))*(
            dtout*sy);
81         tfrelLL(nlayLL,c)=1;
82     end
83
84
85 end
86
87     mpr(3)=(sum(sum(relLL))/sum(sum(tfrelLL)))/sy;
88     mpr(4)=((sum(sum(relLL))/sum(sum(tfrelLL)))*R13pdb*(methc13*1e
        -3+1))/sy;
89 end
90
91 % High Latitude MH Dissociation
92 % -----
93 THL=HL(1,:)+273.15; %Ocean temperature HL (Kelvin)
94 SHL=HL(2,:); %Ocean salinity HL
95
96
97 for nlayHL=4:14
98     P=(1+([dm/2 dm+(1:n-1)*d-d/2])/10)/10; %Pressure [MPa]
99     PdisHL(nlayHL)=(exp(-1.6444866*10.^3-0.1374178*THL(nlayHL)
        +(5.4979866*10.^4/THL(nlayHL))+2.64118188*10.^2*log(THL(nlayHL)
        )+SHL(nlayHL)*(1.1178266*10.^4+7.67420344*THL(nlayHL)
        -4.515213*10.^-3*THL(nlayHL).^2-(2.04872879*10.^5/THL(nlayHL))
        -2.17246046*10.^3*log(THL(nlayHL)))+SHL(nlayHL)
        .*2*(1.70484431*10.^2+0.118594073*THL(nlayHL)-7.0581304*10.^-5*
        THL(nlayHL).^2-(3.09796169*10.^3/THL(nlayHL))-33.2031996*log(
        THL(nlayHL))))); %Hydrate dissociation pressure [MPa]
100    lnSolEq(nlayHL)=-2.5640213*10^5-1.6448053*10^2*THL(nlayHL)
        +9.1089042*10^-2*THL(nlayHL)^2+4.90352929*10^6/THL(nlayHL)

```

```

+4.93009113*10^4*log(THL(nlayHL))+SHL(nlayHL)
*(-5.16285134*10^2-0.33622376*THL(nlayHL)+1.88199047*10^-4*THL(
nlayHL)^2+9.76525718*10^3/THL(nlayHL)+9.9523354*10^1*log(THL(
nlayHL)));
101 Sol(nlayHL)=exp(lnSolEq(nlayHL)+(5.04597*10.^-2+7.64415*10.^-4*SHL(
nlayHL)-(3.90236*10^-4+5.48947*10.^-6*SHL(nlayHL))*THL(nlayHL)
+(7.06154*10.^-7+9.87742*10.^-9*SHL(nlayHL))*THL(nlayHL).^2)*(P
(nlayHL)-PdisHL(nlayHL)))+(7.57285*10.^-5-1.90867*10.^-8*SHL(
nlayHL)-1.4483*10.^-10*SHL(nlayHL)
.^2-(1.96207*10.^-7-6.67456*10.^-11*SHL(nlayHL))*THL(nlayHL))*(
P(nlayHL)-PdisHL(nlayHL)).^2); %Hydrate solubility [mol C/kg]
102 VwHL=aLL.*GAc.*dv; % Volume of water in ocean layer [m3]
103 Dw=1028; % Density water [kg/m3]
104
105
106 if P(nlayHL) < PdisHL(nlayHL)
107
108     if Sol(nlayHL)*VwHL(nlayHL)*Dw>(MHtot*0.16)/(14-4) && trelHL(
nlayHL)==0
109         trelHL(nlayHL)=t;
110         tstopHL(nlayHL)=trelHL(nlayHL)+reltimeHL(nlayHL);
111
112         if trelHL(nlayHL)<=dtout*sy
113             reltimeHL(nlayHL)=tend*sy;
114             tstopHL(nlayHL)=trelHL(nlayHL)+tend*sy;
115         end
116     end
117
118     if dtout*sy > reltimeHL(nlayHL) && trelHL(nlayHL) >0 && t<
tstopHL(nlayHL)
119         relHL(nlayHL,c)=(MHtot*0.16)/(14-4);
120     end
121
122     if trelHL(nlayHL) >0 && tstopHL(nlayHL)>dtout*sy && t<tstopHL(
nlayHL) && sum(relHL(nlayHL,:),2) < (MHtot*0.16)/(14-4)
123         relHL(nlayHL,c)=((MHtot*0.16)/(14-4))/reltimeHL(nlayHL))*
(dtout*sy);
124         tfrelHL(nlayHL,c)=1;
125     end
126 end
127
128 mpr(5)=(sum(sum(relHL))/sum(sum(tfrelHL)))/sy;
129 mpr(6)=((sum(sum(relHL))/sum(sum(tfrelHL)))*R13pdb*(methc13*1e
-3+1))/sy;
130
131 end
132 return

```

## Appendix II: Key Variables Results

In the attached Excel files: AppendixII-A2(5C), AppendixII-A2(3C), AppendixII-B1(5C), AppendixII-B1(3C), the variables selected for model simulation, methane hydrate release in low- and high latitude ocean layers, end-values for ocean tracers as a function of depth in low- and high latitude, and end-values for atmospheric tracers in low- and high latitude are included for the scenario.

### A2(5°C)

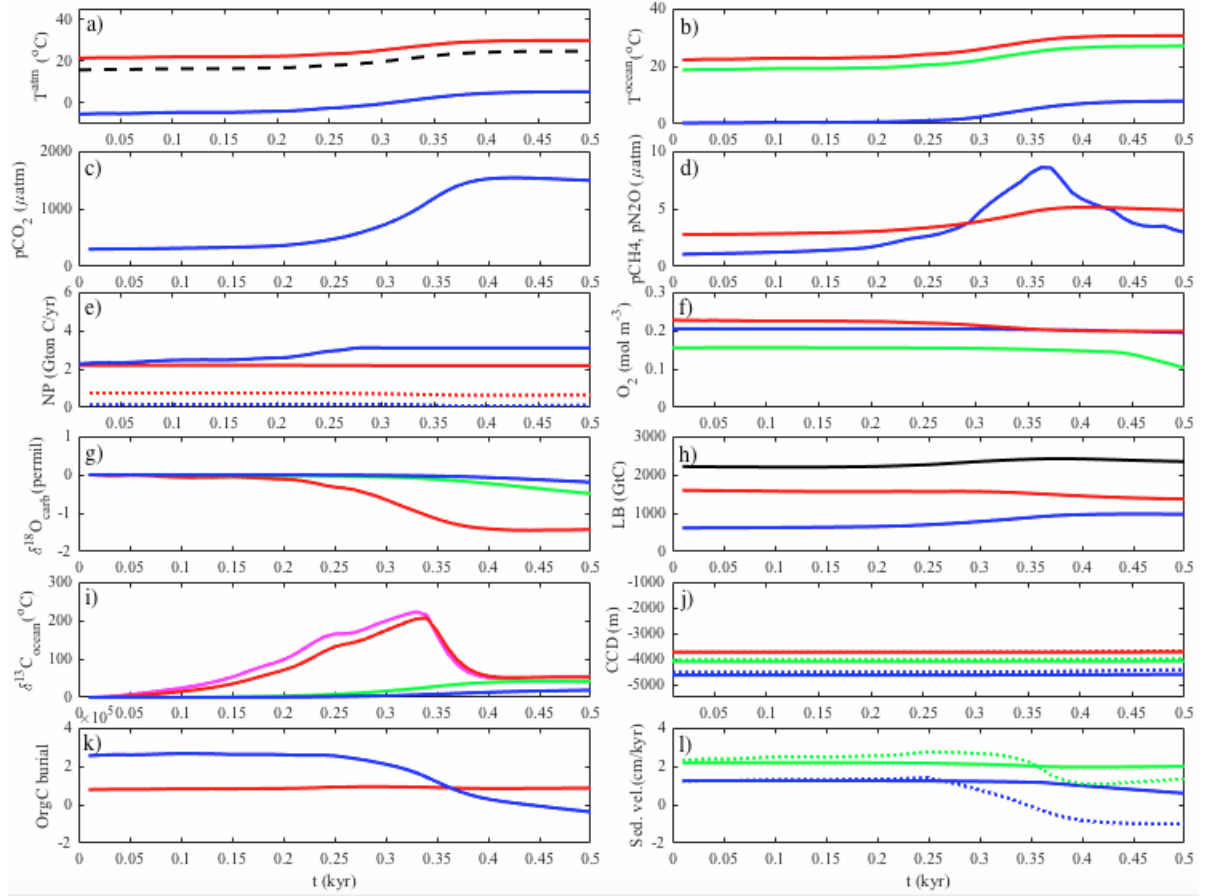


Figure 28: A2 scenario with 5°C sensitivity

Results from a 500 year model simulation of A2 scenario with 5°C sensitivity, with a methane input of 63 Gt C. **a)** Mean atmospheric temperature in low latitude (red) and high latitude (blue) sectors, together with the global mean temperature (black). **b)** Mean ocean temperature in low latitude (red) and high latitude (blue) sectors, together with the global mean ocean temperature (green). **c)** Atmospheric partial pressure of carbon dioxide. **d)** Atmospheric partial pressure of methane (blue) and nitrous oxide (red). **e)** Ocean new production in low latitude (red) and high latitude (blue) zones. **f)** Dissolved  $\text{O}_2$  concentration in low latitude ocean at 100 meters (red), 1000 meters (blue) and 3000 meters (green) depth. **g)** Low latitude excursions of  $\delta^{18}$  in biogenic  $\text{CaCO}_3$  at 100 meters (red), 1000 meters (blue), and 3000 meters (green) depth. **h)** Land biosphere of leaf and wood biomass carbon (blue), Litter and soil biomass carbon (red) and total biomass carbon (black). **i)**  $\delta^{13}\text{C}$  Carbon isotope excursion for the atmosphere (pink) and low latitude ocean at 100 meters (red), 1000 meters (blue), 3000 meters (green) depth. **j)** Carbonate compensation depth for low latitude (continuous lines) and high latitude (dotted lines), at 1000 meters

(blue), 3000 meters (green) and 5000 meters (red) depth. **k)** Organic carbonate burial (red) and Carbonate carbon burial (blue). **l)** Sedimentation velocity in low latitude (continuous lines) and high latitude (dotted lines) sectors at 1000 meters (green) and 3000 meters (blue) depth.

## A2(3°C)

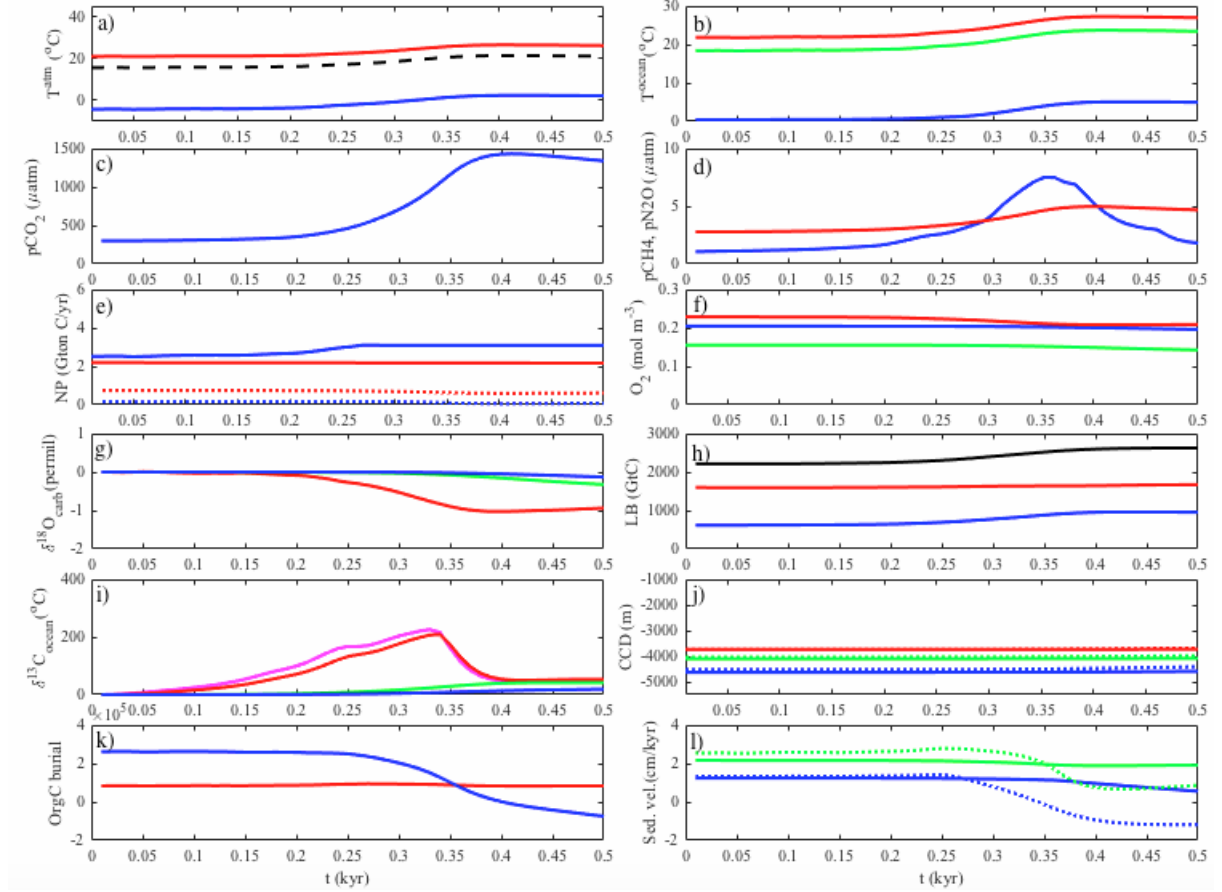


Figure 29: A2 scenario with 3°C sensitivity

Results from a 500 year model simulation of A2 scenario with 3°C sensitivity, with a methane input of 63 Gt C. **a)** Mean atmospheric temperature in low latitude (red) and high latitude (blue) sectors, together with the global mean temperature (black). **b)** Mean ocean temperature in low latitude (red) and high latitude (blue) sectors, together with the global mean ocean temperature (green). **c)** Atmospheric partial pressure of carbon dioxide. **d)** Atmospheric partial pressure of methane (blue) and nitrous oxide (red). **e)** Ocean new production in low latitude (red) and high latitude (blue) zones. **f)** Dissolved O<sub>2</sub> concentration in low latitude ocean at 100 meters (red), 1000 meters (blue) and 3000 meters (green) depth. **g)** Low latitude excursions of  $\delta^{18}\text{O}_{\text{carb}}$  in biogenic CaCO<sub>3</sub> at 100 meters (red), 1000 meters (blue), and 3000 meters (green) depth. **h)** Land biosphere of leaf and wood biomass carbon (blue), Litter and soil biomass carbon (red) and total biomass carbon (black). **i)**  $\delta^{13}\text{C}$  Carbon isotope excursion for the atmosphere (pink) and low latitude ocean at 100 meters (red), 1000 meters (blue), 3000 meters (green) depth. **j)** Carbonate compensation depth for low latitude (continuous lines) and high latitude (dotted lines), at 1000 meters (blue), 3000 meters (green) and 5000 meters (red) depth. **k)** Organic carbonate burial (red) and Carbonate carbon burial (blue). **l)** Sedimentation velocity in low latitude (continuous lines) and high latitude (dotted

lines) sectors at 1000 meters (green) and 3000 meters (blue) depth.

### B1(5°C)

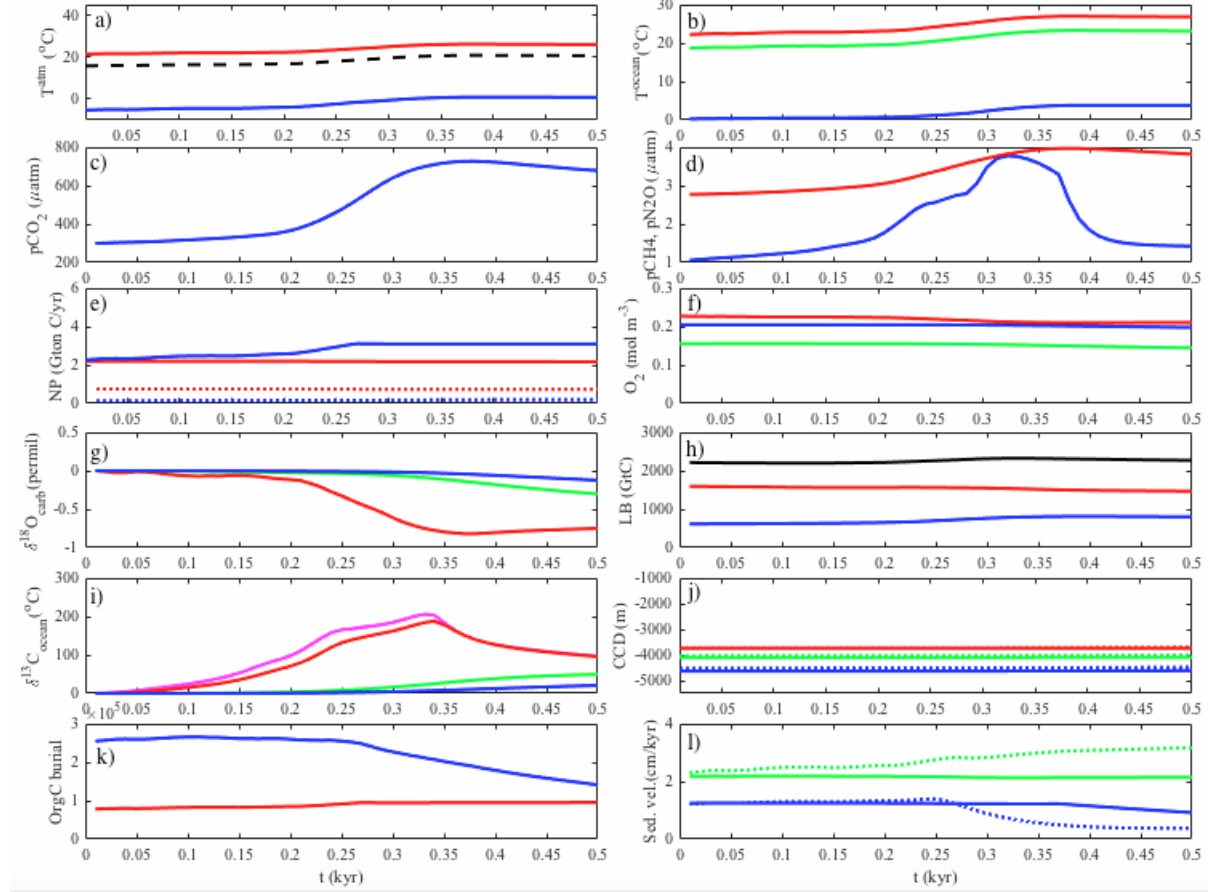


Figure 30: B1 scenario with 5°C sensitivity

Results from a 500 year model simulation of B1 scenario with 5°C sensitivity, with a methane input of 63 Gt C. **a)** Mean atmospheric temperature in low latitude (blue) sectors, together with the global mean temperature (black). **b)** Mean ocean temperature in low latitude (red) and high latitude (blue) sectors, together with the global mean ocean temperature (green). **c)** Atmospheric partial pressure of carbon dioxide. **d)** Atmospheric partial pressure of methane (blue) and nitrous oxide (red). **e)** Ocean new production in low latitude (red) and high latitude (blue) zones. **f)** Dissolved O<sub>2</sub> concentration in low latitude ocean at 100 meters (red), 1000 meters (blue) and 3000 meters (green) depth. **g)** Low latitude excursions of  $\delta^{18}\text{O}_{\text{carb}}$  in biogenic CaCO<sub>3</sub> at 100 meters (red), 1000 meters (blue), and 3000 meters (green) depth. **h)** Land biosphere of leaf and wood biomass carbon (blue), Litter and soil biomass carbon (red) and total biomass carbon (black). **i)**  $\delta^{13}\text{C}$  Carbon isotope excursion for the atmosphere (pink) and low latitude ocean at 100 meters (red), 1000 meters (blue), 3000 meters (green) depth. **j)** Carbonate compensation depth for low latitude (continuous lines) and high latitude (dotted lines), at 1000 meters (blue), 3000 meters (green) and 5000 meters (red) depth. **k)** Organic carbon burial (red) and Carbonate carbon burial (blue). **l)** Sedimentation velocity in low latitude (continuous lines) and high latitude (dotted lines) sectors at 1000 meters (green) and 3000 meters (blue) depth.

## B1(3°C)

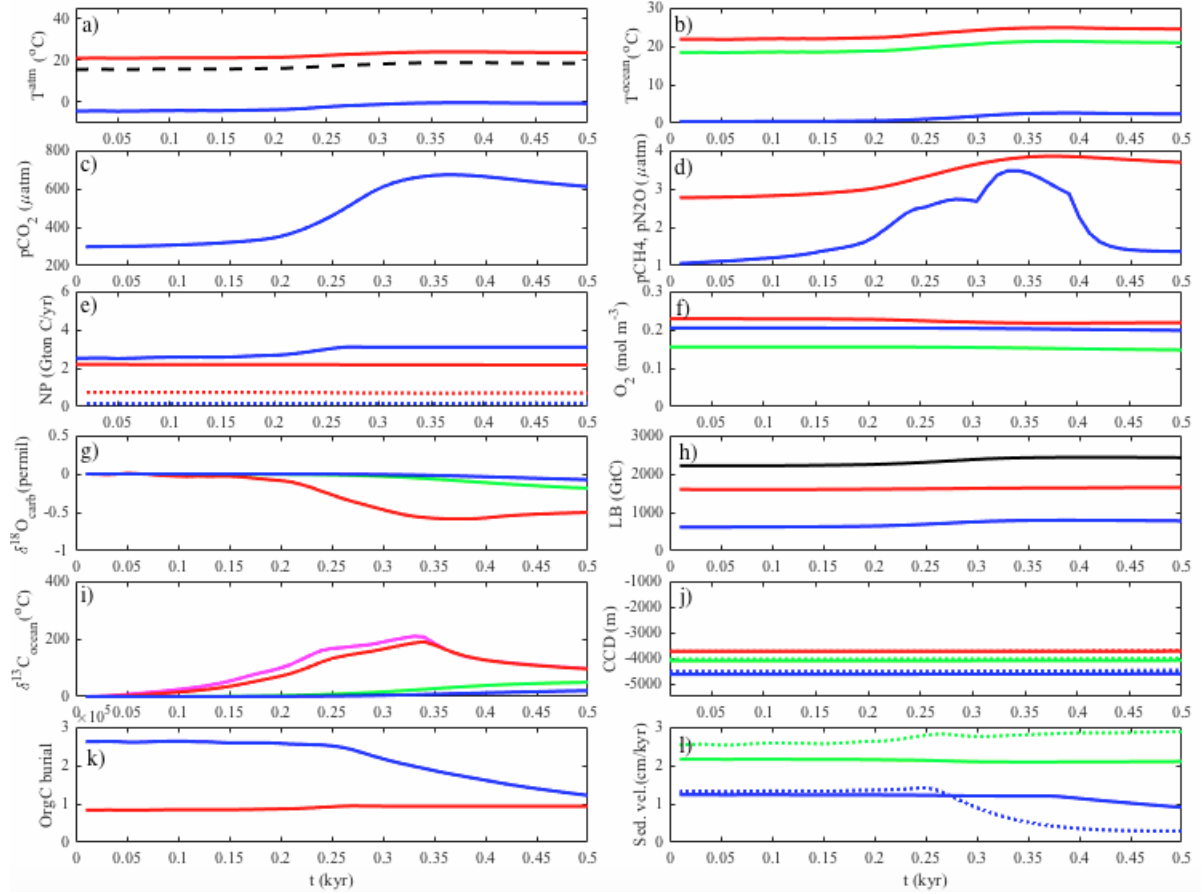


Figure 31: B1 scenario with 3°C sensitivity

Results from a 500 year model simulation of B1 scenario with 3°C sensitivity, with a methane input of 63 Gt C. **a)** Mean atmospheric temperature in low latitude (red) and high latitude (blue) sectors, together with the global mean temperature (black). **b)** Mean ocean temperature in low latitude (red) and high latitude (blue) sectors, together with the global mean ocean temperature (green). **c)** Atmospheric partial pressure of carbon dioxide. **d)** Atmospheric partial pressure of methane (blue) and nitrous oxide (red). **e)** Ocean new production in low latitude (red) and high latitude (blue) zones. **f)** Dissolved O<sub>2</sub> concentration in low latitude ocean at 100 meters (red), 1000 meters (blue) and 3000 meters (green) depth. **g)** Low latitude excursions of  $\delta^{18}\text{O}_{\text{carb}}$  in biogenic CaCO<sub>3</sub> at 100 meters (red), 1000 meters (blue), and 3000 meters (green) depth. **h)** Land biosphere of leaf and wood biomass carbon (blue), Litter and soil biomass carbon (red) and total biomass carbon (black). **i)**  $\delta^{13}\text{C}$  Carbon isotope excursion for the atmosphere (pink) and low latitude ocean at 100 meters (red), 1000 meters (blue), 3000 meters (green) depth. **j)** Carbonate compensation depth for low latitude (continuous lines) and high latitude (dotted lines), at 1000 meters (blue), 3000 meters (green) and 5000 meters (red) depth. **k)** Organic carbonate burial (blue) and Carbonate carbon burial (red). **l)** Sedimentation velocity in low latitude (continuous lines) and high latitude (dotted lines) sectors at 1000 meters (green) and 3000 meters (blue) depth.

### **Appendix III: Zero Methane Hydrate**

In the Attached Excel file: AppendixIII-ZeroMethane, the comparison between the model run with methane hydrate inventory  $> 0$  and methane hydrate inventory  $= 0$  is included for all scenarios: A2(5°C), A2(3°C), B1(5°C) and B1(3°C).

## Appendix IV: Sensitivity Analysis

### Methane Hydrate Inventory

In the attached Excel file: AppendixIV-InventorySize(A2(5C)), information regarding the following subjects in the sensitivity analysis of methane hydrate inventory are included:

1. Sensitivity analysis for methane hydrate inventory size (linear regression)
2. Sensitivity analysis with regards the atmospheric tracers  $pCO_2$ ,  $pCH_4$  and  $t_{atm}$

### Total Release Time

As the DCESS model operates with a twofolded ocean module with regards to latitude, the reservoir is divided in two segments, with 84 % of the  $CH_4$  inventory located in low latitude ocean and 16 % in high latitude ocean. Furthermore, the respective high latitude and low latitude reservoirs are distributed in ocean layers located between 300 and 1200 meters depth.

The current  $CH_4$  inventory is estimated to 1800 Gt C (Ruppel and Kessler, 2016). The contemporary global  $CH_4$  flux in the interface between the sediments and the overlaying water column is between 16 and 3200 Tg  $CH_4$  per year. This range is based on a balancing of  $CH_4$  emissions to the water column by aerobic  $CH_4$  oxidation with first order MOx rate constants between 0.001 and 0.2 per day (Ruppel and Kessler, 2016). Hence, the average contemporary flux is 1608 Tg C per year. The reservoir size and average release rate allow the estimation of the contemporary total release time parameter,

$$RT_{HL}/RT_{LL} = \frac{MH_{totHL}/MH_{totLL}}{q} \quad (21)$$

where RT is the total release time per layer in years,  $MH_{tot}$  is the reservoir size in Tg  $CH_4$  per layer and q is the average flux in Tg  $CH_4$  per year. The underscore HL and LL indicate high latitude and low latitude, respectively. The resulting total release time is in the range between 0.5 and 90 years in high latitudes. The total release time in low latitudes exists in the range between 0.5 and 140 years. The total release time based on contemporary values is used as a indicator, and is expected to decrease with increased  $CH_4$  flux.

Equation 22 and Equation 23 show the calculation of maximum and minimum contemporary release time in high latitudes:

$$RT_{maxHL} = \frac{\frac{63*GtC*0.16*\frac{23.70Tg}{GtC}}{14-4*Layer}}{\frac{\frac{16Tg}{Year}*0.16}{14-4Layer}} = 93.3187500Year \quad (22)$$

$$RT_{minHL} = \frac{\frac{63*GtC*0.16*\frac{23.70Tg}{GtC}}{14-4*Layer}}{\frac{\frac{3200Tg}{Year}*0.16}{14-4Layer}} = 0.4665937500Year \quad (23)$$

Equation 24 and Equation 25 show the calculation of maximum and minimum contemporary release time in low latitudes:

$$RT_{maxLL} = \frac{\frac{63*GtC*0.84*\frac{23.70Tg}{GtC}}{14-8*Layer}}{\frac{\frac{16Tg}{Year}*0.84}{14-8Layer}} = 139.9781250Year \quad (24)$$

$$RT_{minLL} = \frac{\frac{63*GtC*0.84*\frac{23.70Tg}{GtC}}{14-8*Layer}}{\frac{\frac{3200Tg}{Year}*0.84}{14-8Layer}} = 0.4642723881Year \quad (25)$$

In the attached Excel files: AppendixIV-ReleaseTime10(A2(5C)) and AppendixIV-ReleaseTime50(A2(5C)), the end point variable values in the ocean and atmosphere for release times of respectively 10 years and 50 years can be extracted.



Cover photo reference: <http://www.bbc.com/news/business-27021610>

DTU Space  
Danmarks Tekniske Universitet  
Elektrovej Bygning 328  
2800 Kongens Lyngby  
[www.space.dtu.dk](http://www.space.dtu.dk)  
June 2017